Astronomical Instrumentation and Data Analysis

Detectors for Astroparticle Physics

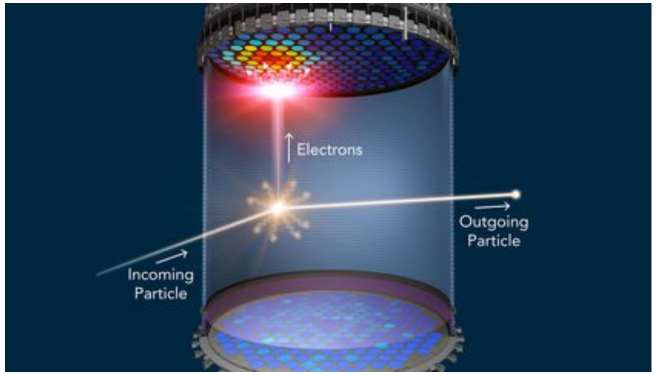

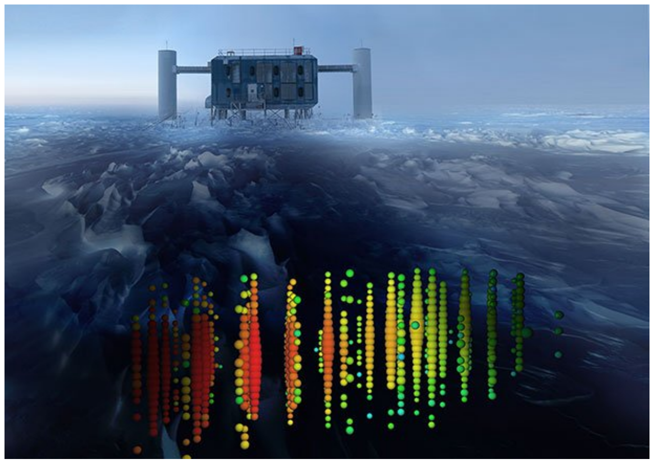

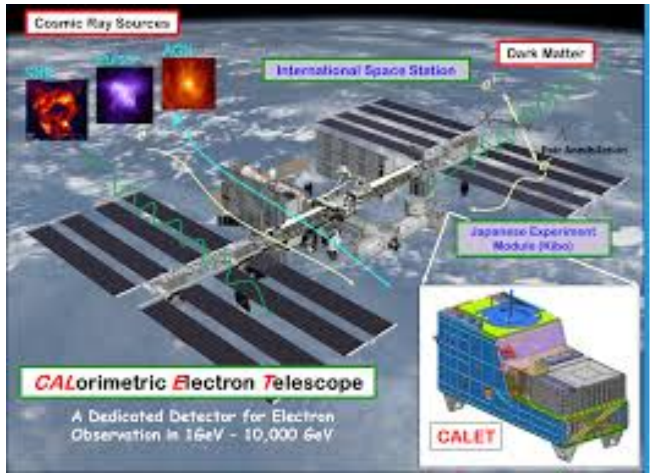

Jörg R. Hörandel
http://particle.astro.ru.nl

Astroparticle Physics

messengers from the Universe

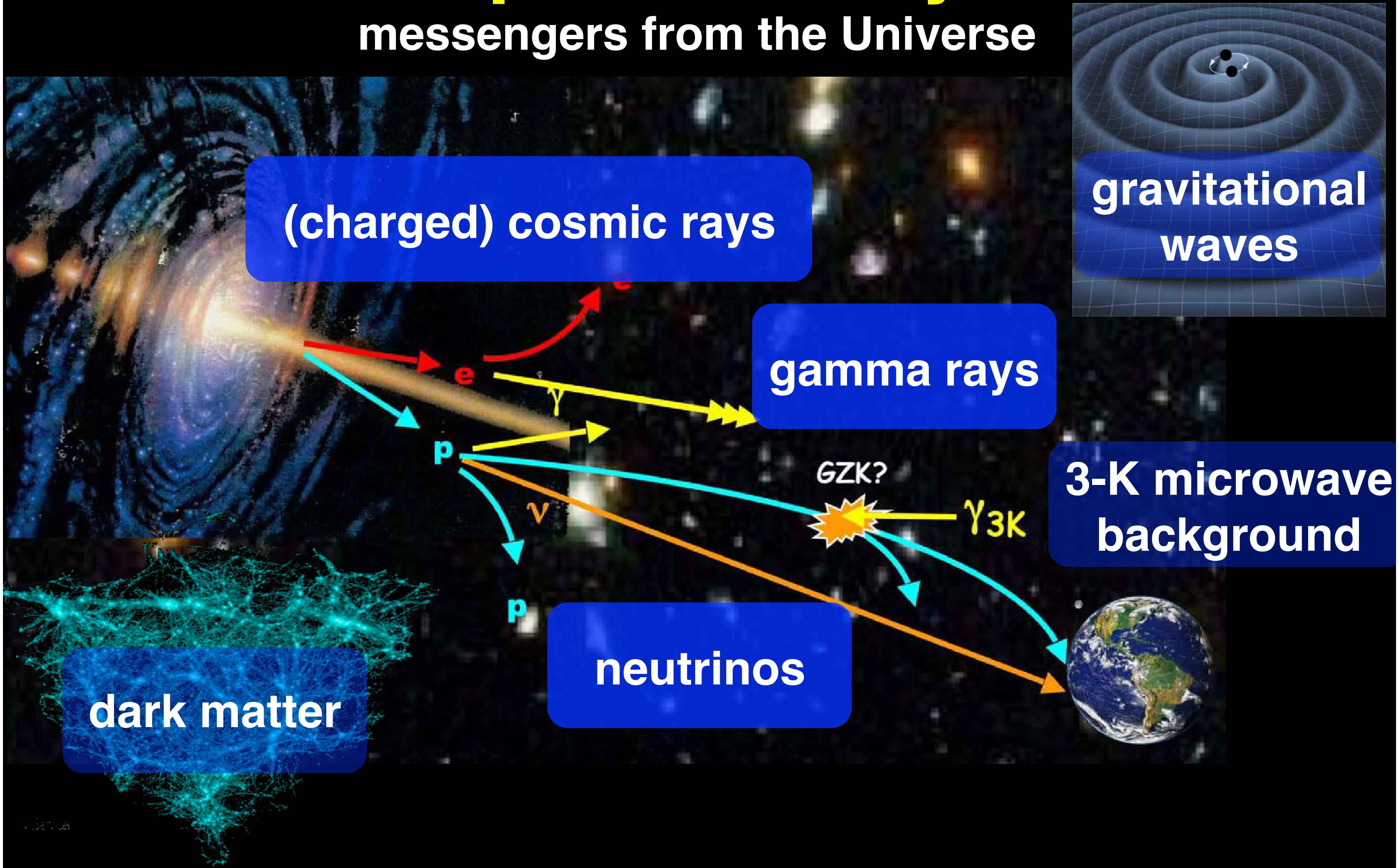

Astronomical Instrumentation and Data Analysis

Detectors for Astroparticle Physics

- (charged) Cosmic Rays
- Gamma Rays
- Neutrinos
- Dark Matter
- Gravitational Waves

Jörg R. Hörandel
http://particle.astro.ru.nl

Radio Emission in Air Showers

- **Mainly: Charge separation in geomagnetic field**
  $\vec{E} \propto \vec{v} \times \vec{B}$

Theory predicts additional mechanisms:

- **excess of electrons in shower: charge excess**
- **superposition of emission due to Cherenkov effects in atmosphere**

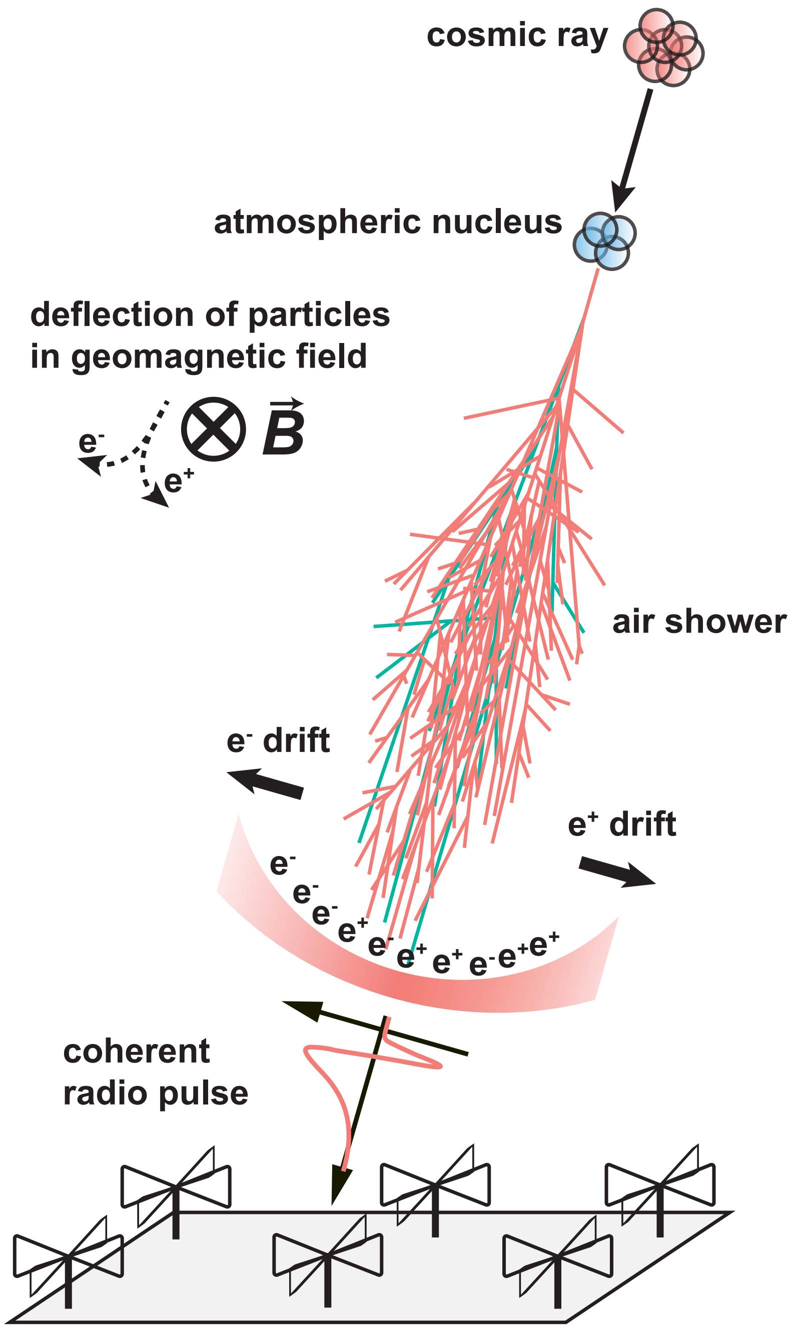

polarization of radio signal

geomagnetic

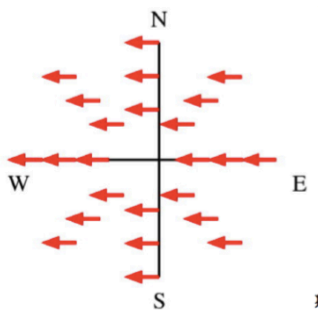

Askaryan

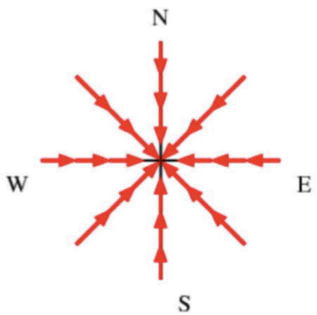

Radio detection of extensive air showers around the world

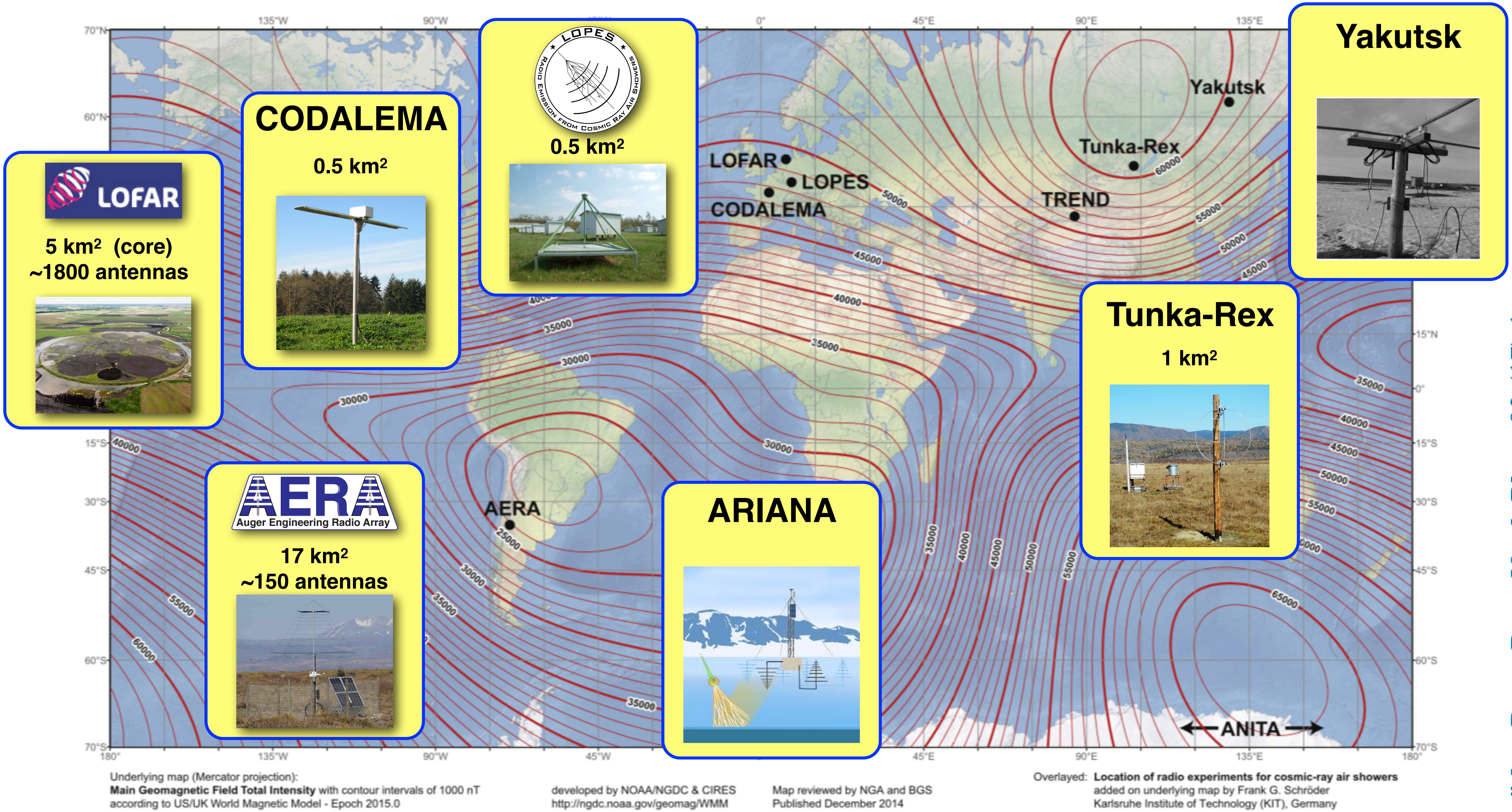

Fig. 21. Map of the total geomagnetic field strengths (world magnetic model [207]) and the location of various radio experiments detecting cosmic-ray air showers.

F.G. Schröder, Prog. Part. Nucl. Phys. 92 (17) 1

LOPES
Lofar Prototype Station

30 antennas operating at KASCADE-Grande

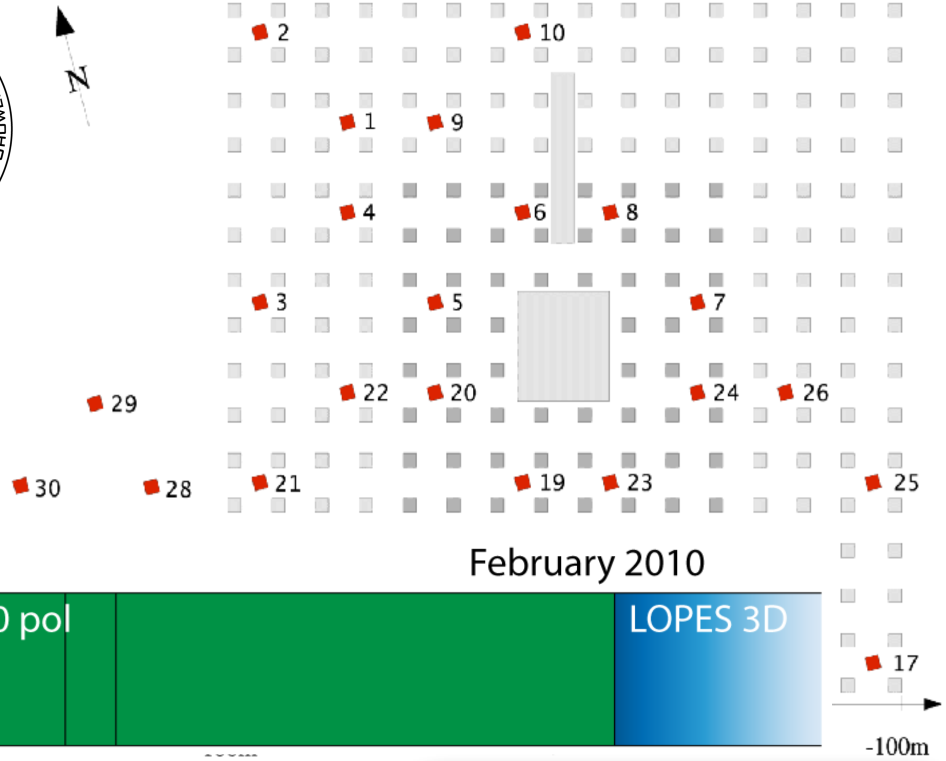

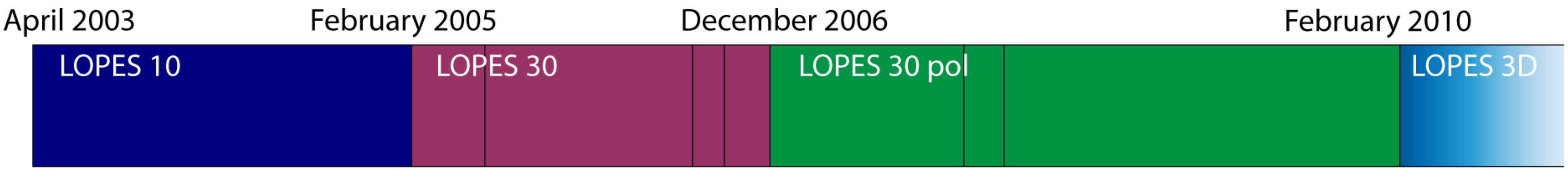

digital radio interferome

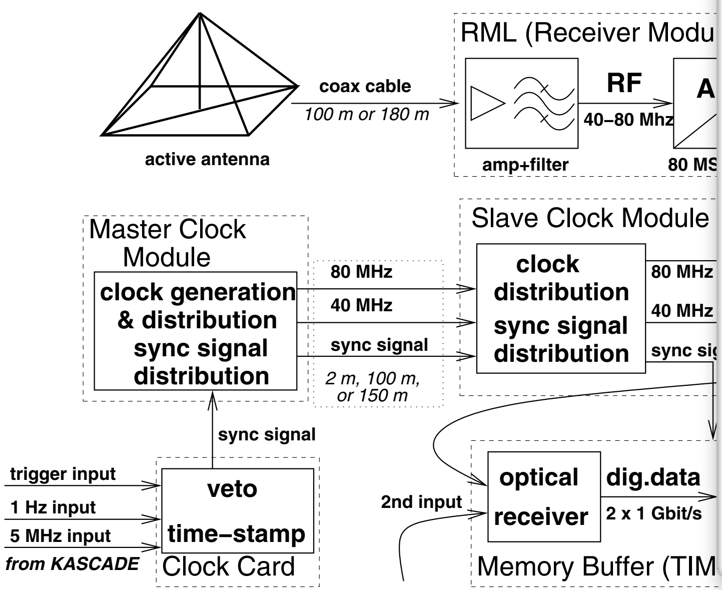

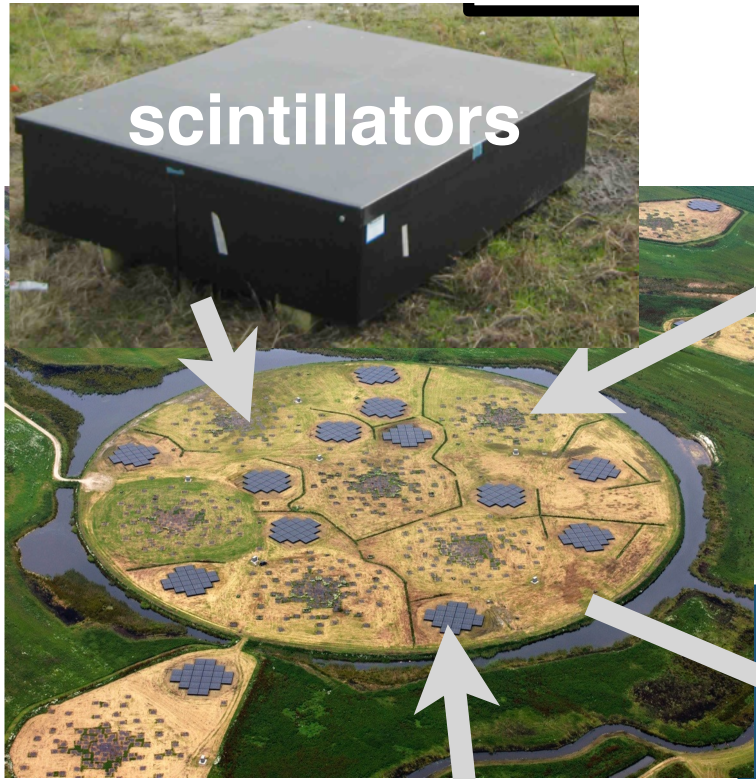

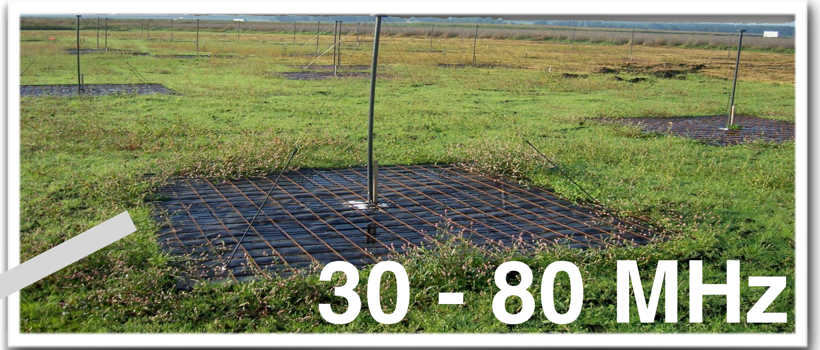

core
23 stations ~5 km^2

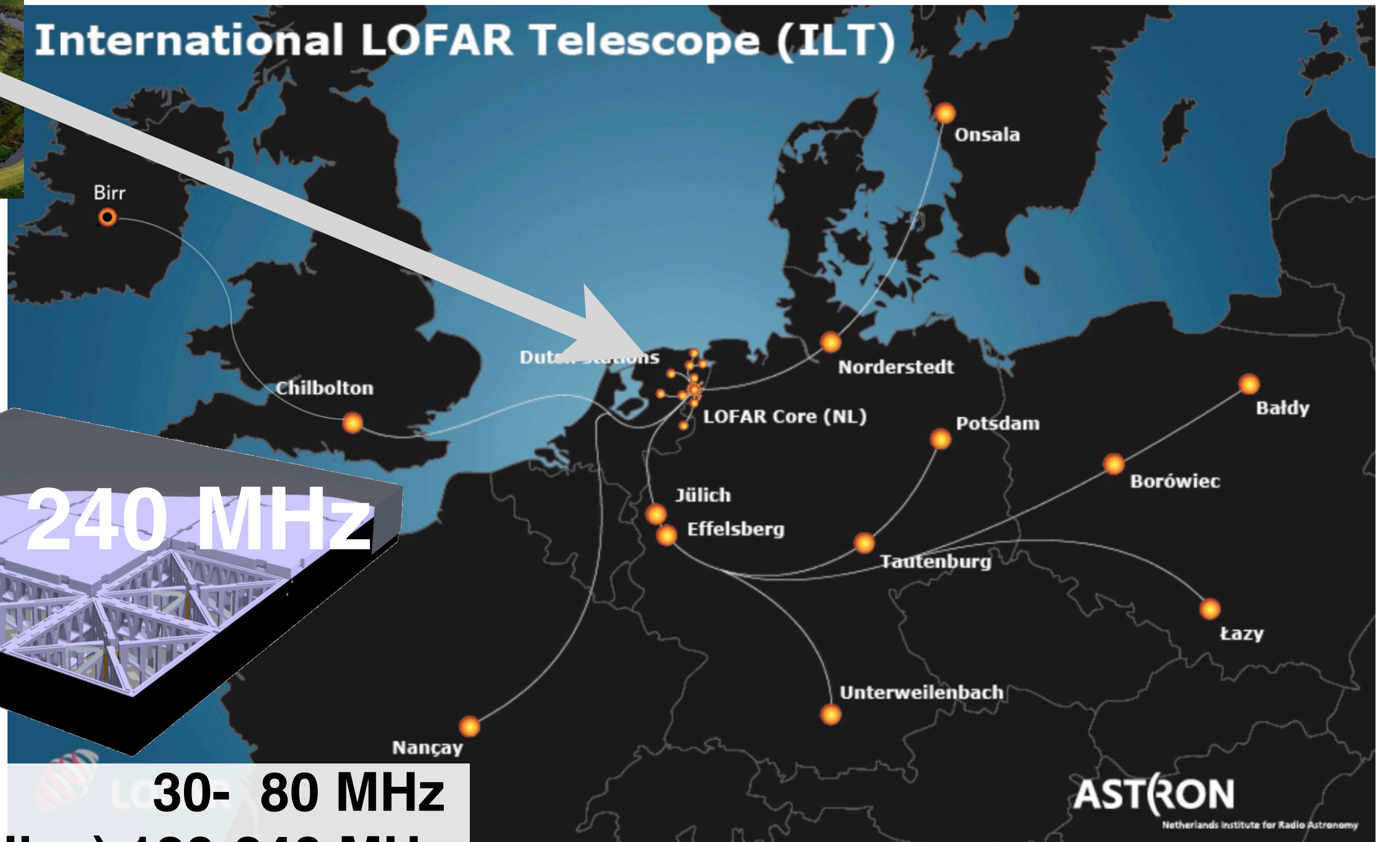

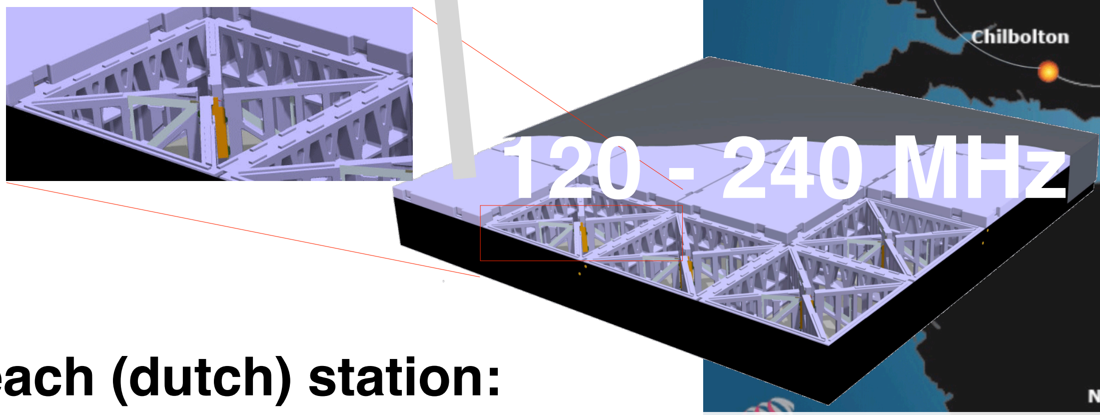

each (dutch) station:
96 low-band antennas 30- 80 MHz
high-band antennas (2x24 tiles) 120-240 MHz

M. van Haarlem et al., A&A 556 (2013) A2

S. Thoudam et al., Nucl. Instr. Meth. A 767 (2014) 339

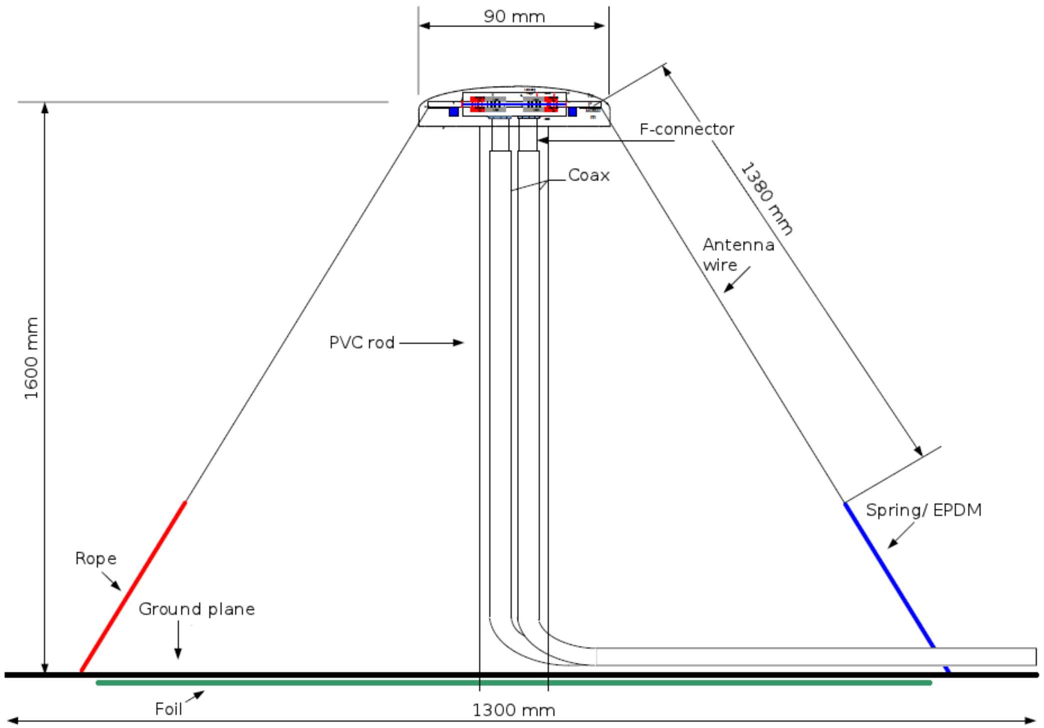

Figure 3.5: Schematic view of the LBA. The pillar is shown in the middle with the LNA on top of it. The dipole wires are located to the right and left of the LBA. Figure taken from [62].

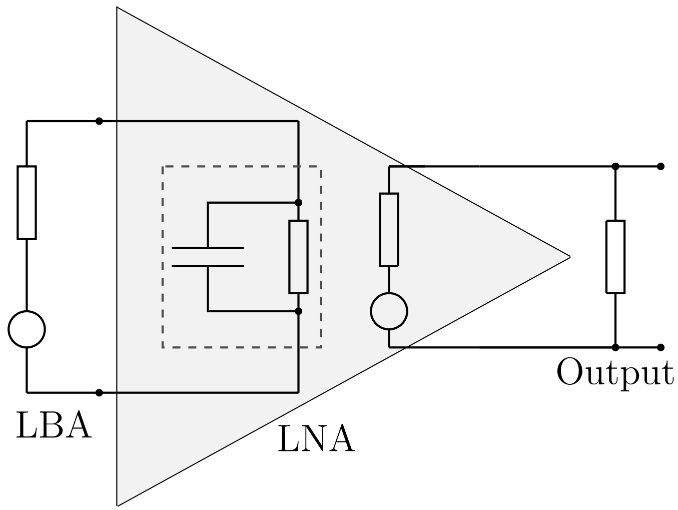

Figure 3.6: Simplified equivalent circuit of the LBA together with the electronics. The LNA works as an operational amplifier.

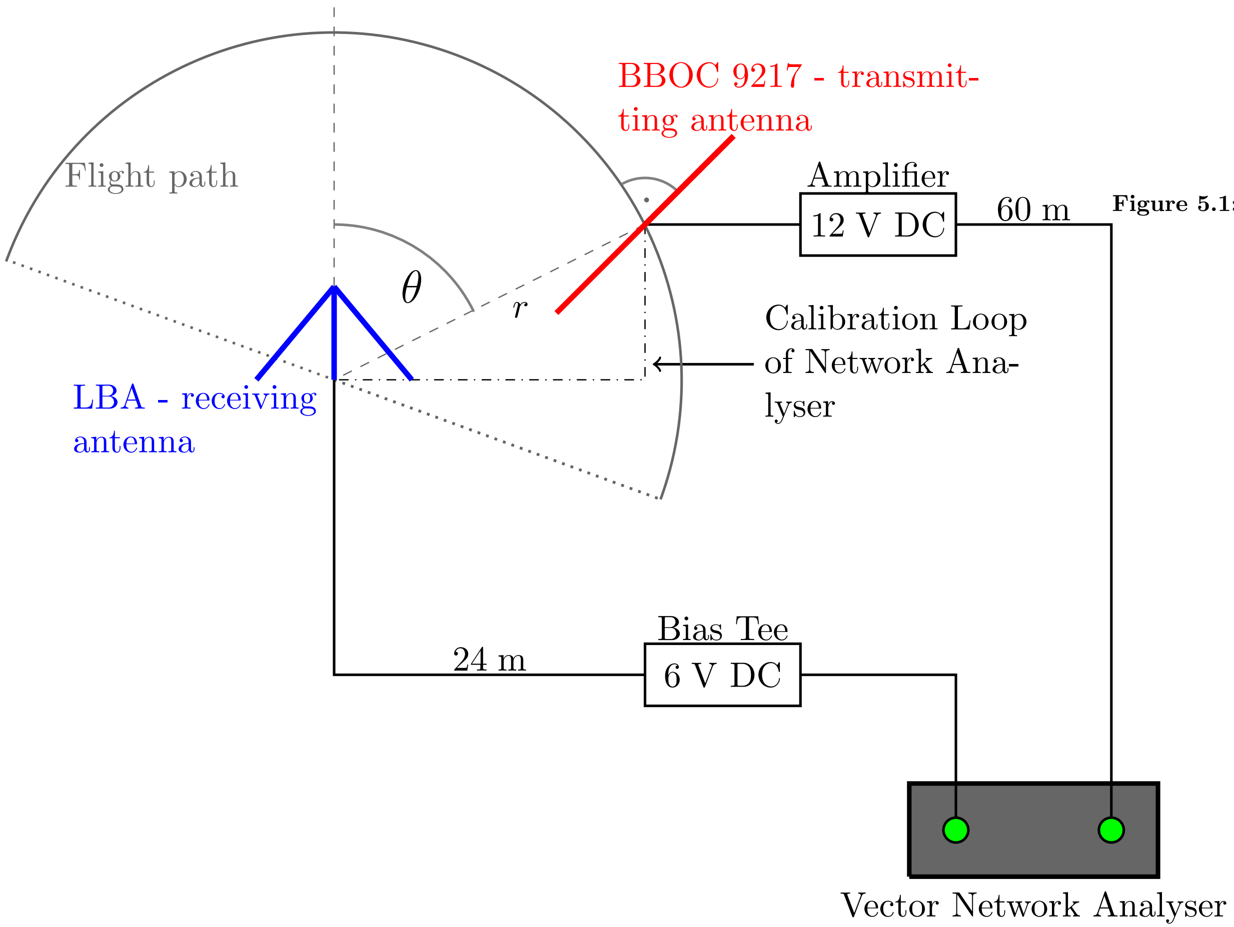

Figure 5.3: Set-up to measure the horizontal gain. The grey half circle denotes the path of the transmitting antenna. The angle θ highlights the zenith angle of the transmitting antenna with respect to the LBA. The black dashed-dotted line indicates the cable connection between the LBA and the amplifier used for the calibration of the network analyser. Modified figure from [41].

Figure 5.1: *Left:* Biconical antenna used for the calibration measurements. *Right:* Octocopter with the transmitting antenna mounted below.

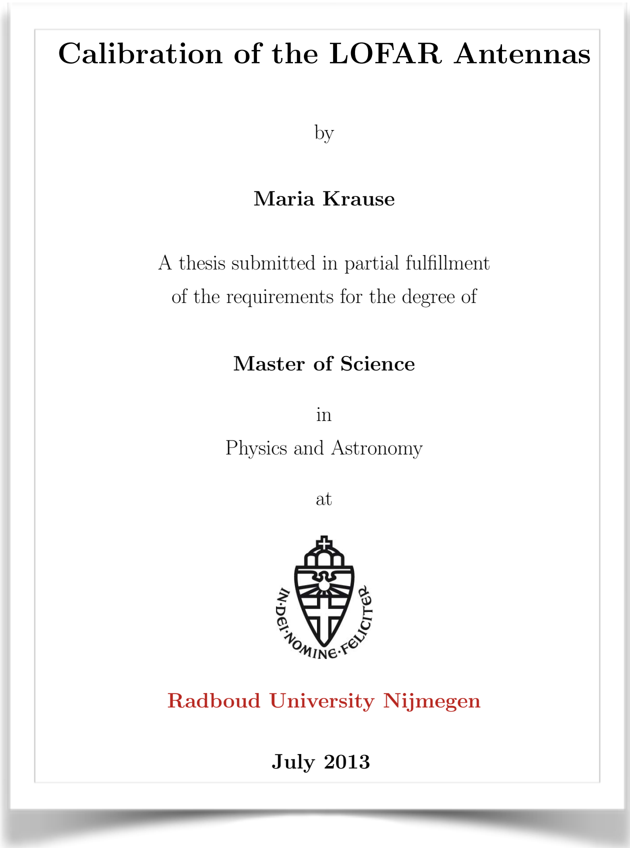

Calibration of the LOFAR Antennas

by

Maria Krause

A thesis submitted in partial fulfillment
of the requirements for the degree of

Master of Science

in
Physics and Astronomy

at

Radboud University Nijmegen

July 2013

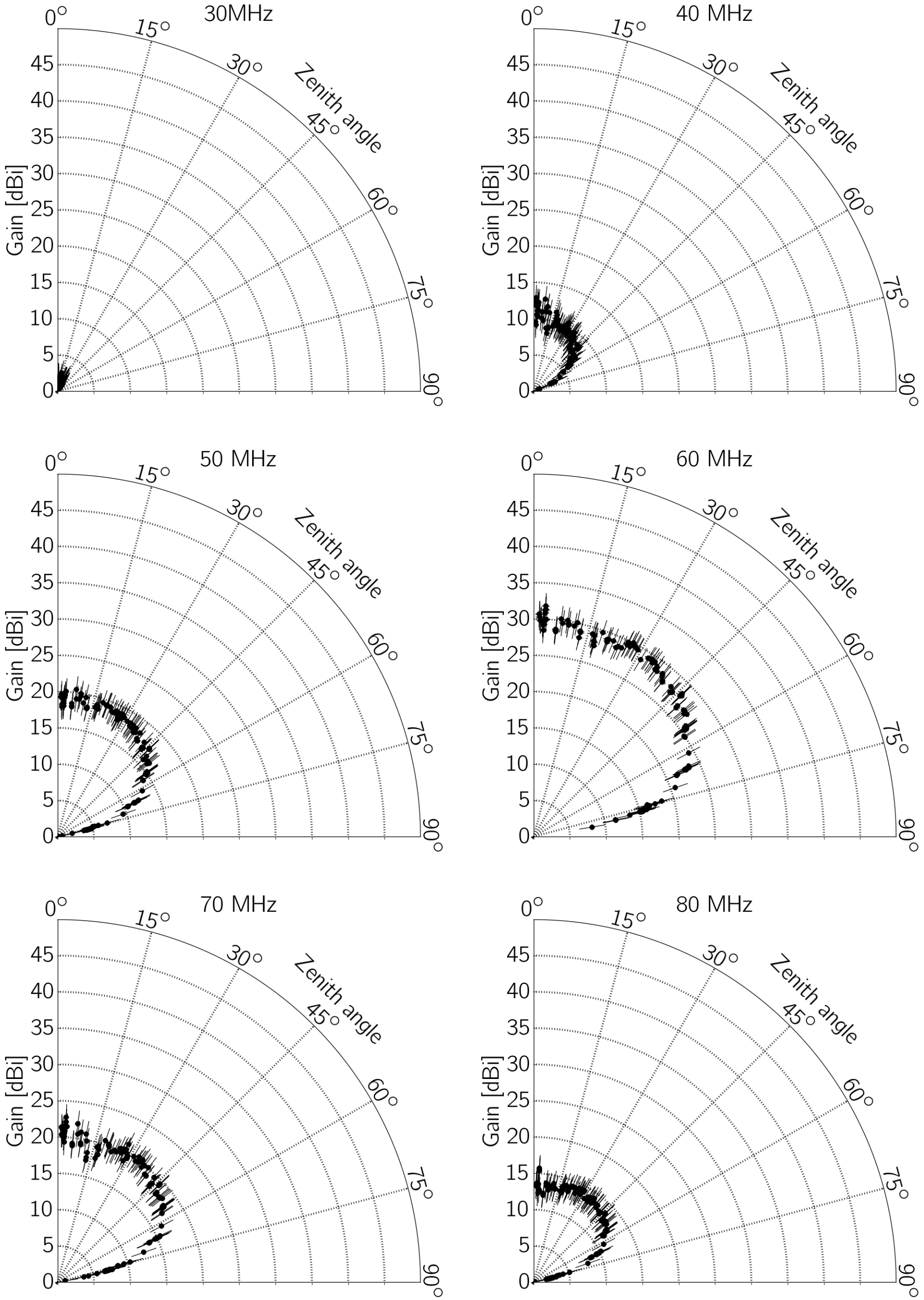

Figure 5.12: Measurements of the horizontal gain of the outer LBA as a function of zenith angle for different frequencies. The error bars indicate the systematic uncertainty caused by the frequency analyser and the biconical antenna. The statistical errors are small compared to the systematic ones. The error bars of the zenith angle are smaller than the marker size.

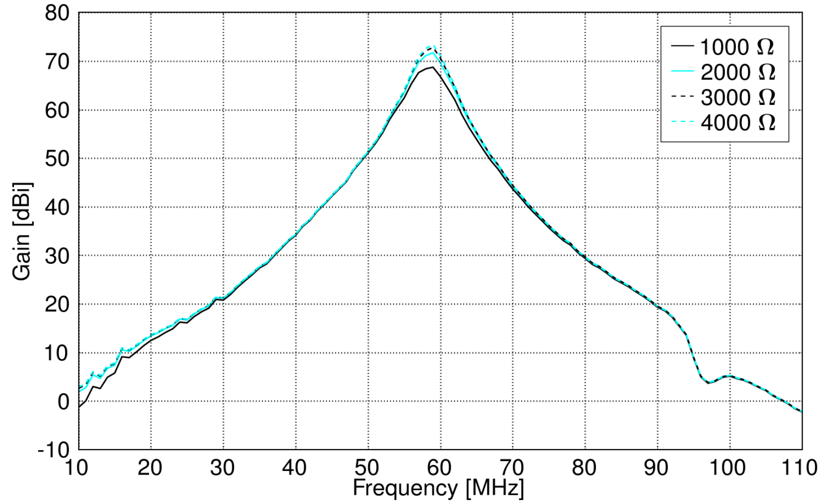

Figure 5.14: Comparison of the simulated gain as a function of frequency for different resistors and a fixed capacitor.

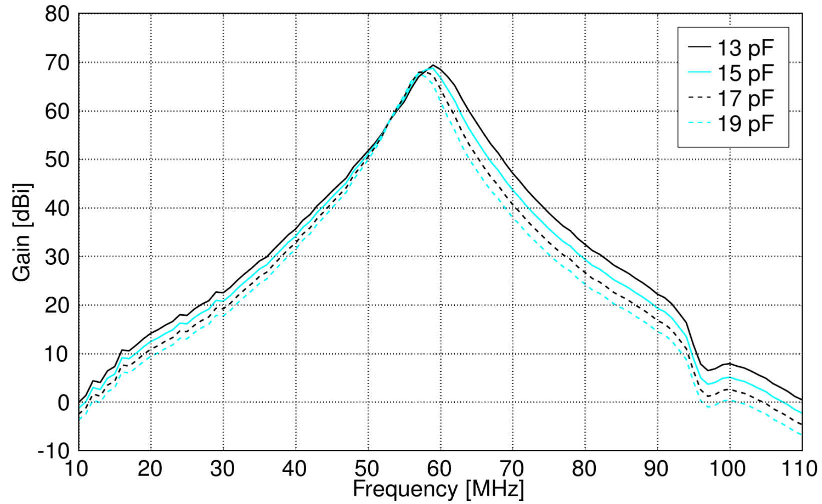

Figure 5.15: Comparison of the simulated gain as a function of frequency for different capacitors and a fixed resistor.

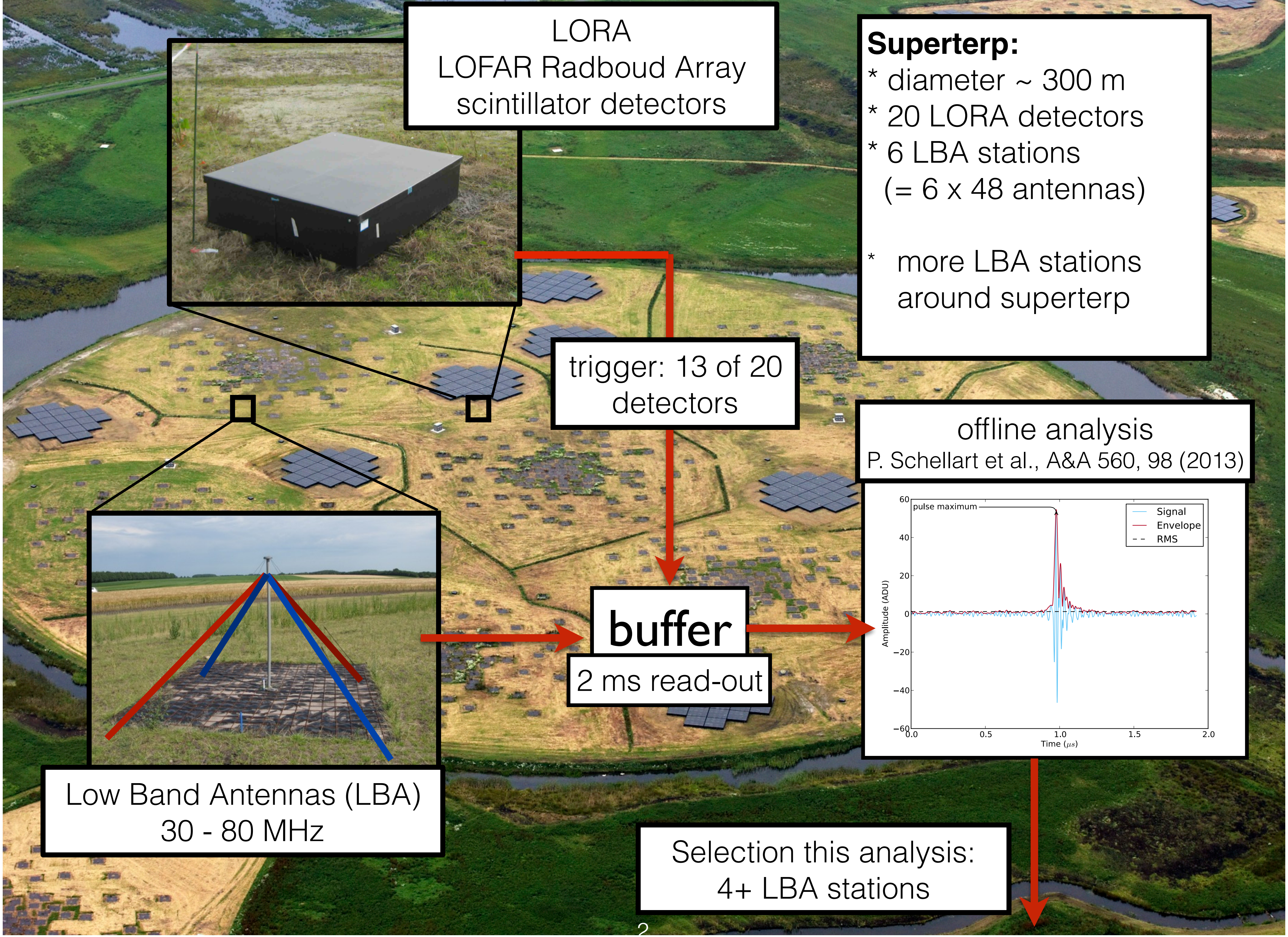
LORA
LOFAR Radboud Array
scintillator detectors
Superterp:
* diameter ~ 300 m
* 20 LORA detectors
* 6 LBA stations
(= 6 x 48 antennas)
* more LBA stations
around superterp
trigger: 13 of 20
detectors
offline analysis
P. Schellart et al., A&A 560, 98 (2013)
pulse maximum
Signal
Envelope
RMS
Amplitude (ADU)
Time (μs)
buffer
2 ms read-out
Low Band Antennas (LBA)
30 - 80 MHz
Selection this analysis:
4+ LBA stations

S. Buitink

PIERRE AUGER OBSERVATORY

AERA
Auger Engineering Radio Array

~150 antennas
~17 km²
30-80 MHz

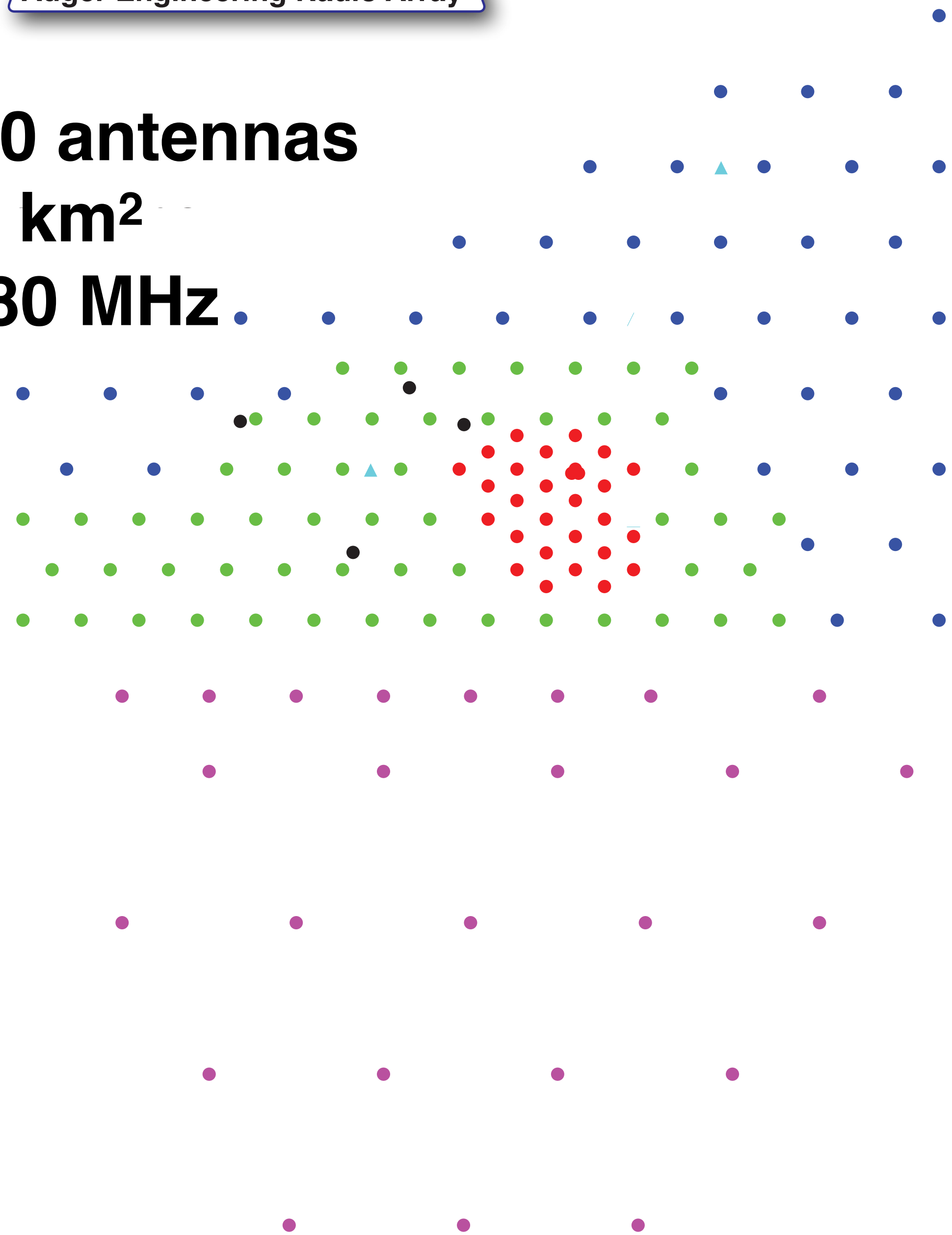

LOFAR core
23 stations ~5 km²

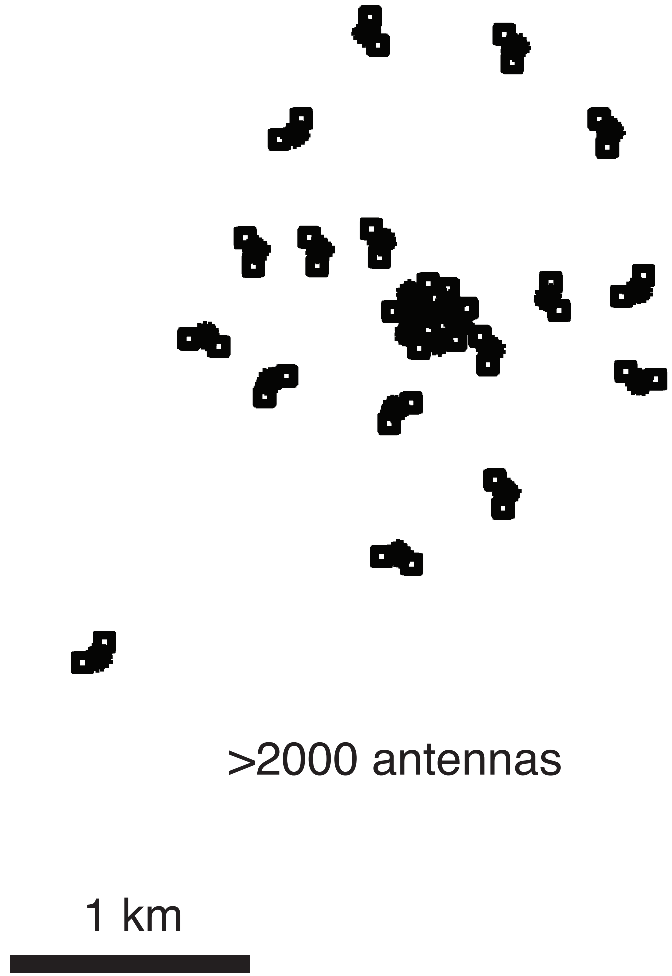

PIERRE AUGER OBSERVATORY

AERA
Auger Engineering Radio Array

~150 antennas
~17 km²
30-80 MHz

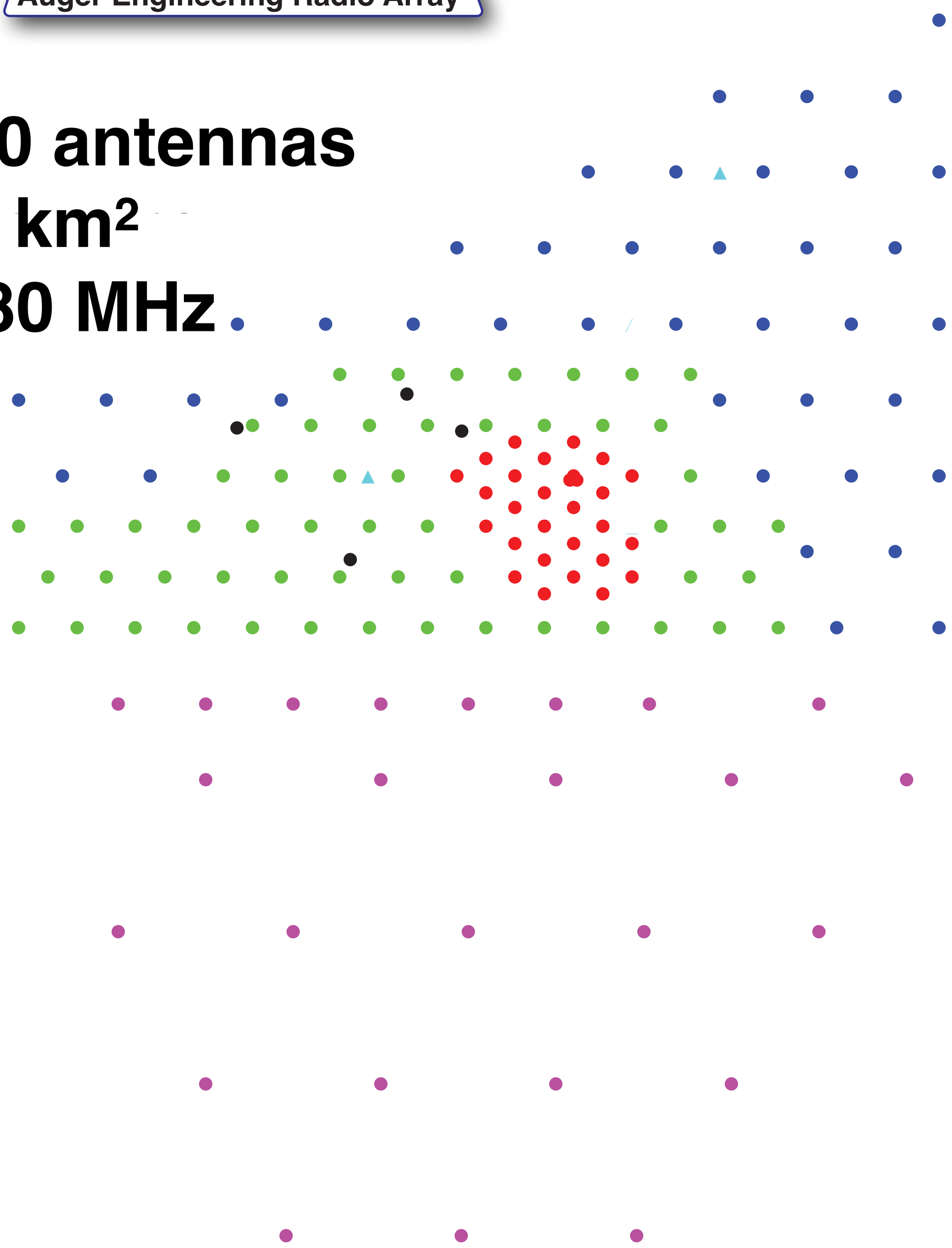

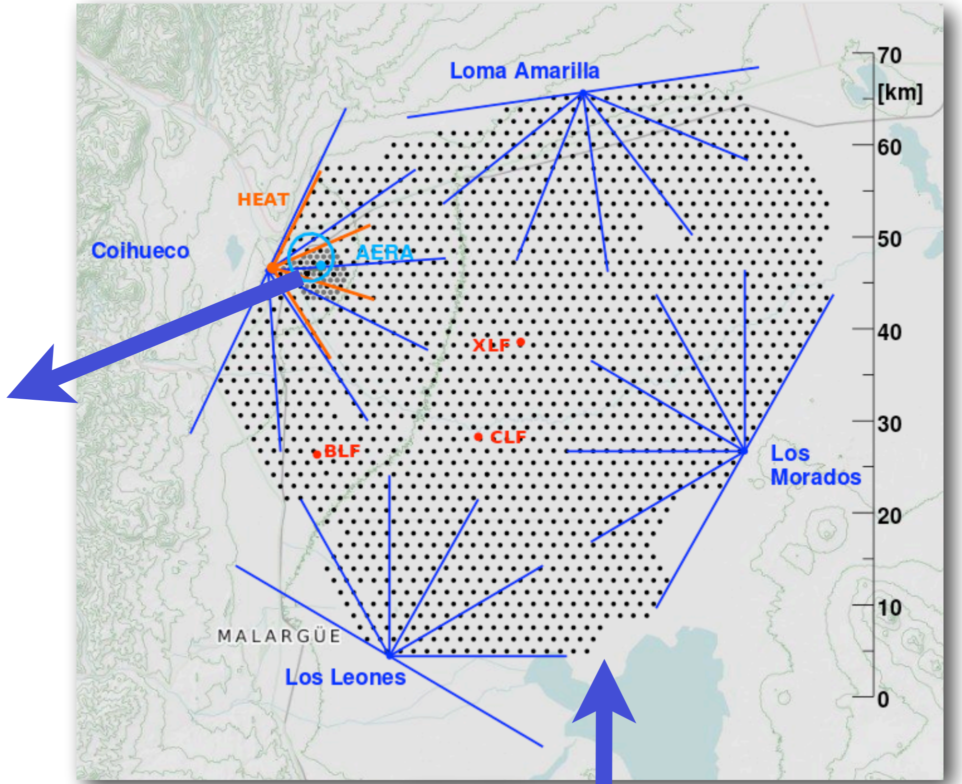

PIERRE AUGER OBSERVATORY

AERA
Auger Engineering Radio Array

~150 antennas
~17 km²
30-80 MHz

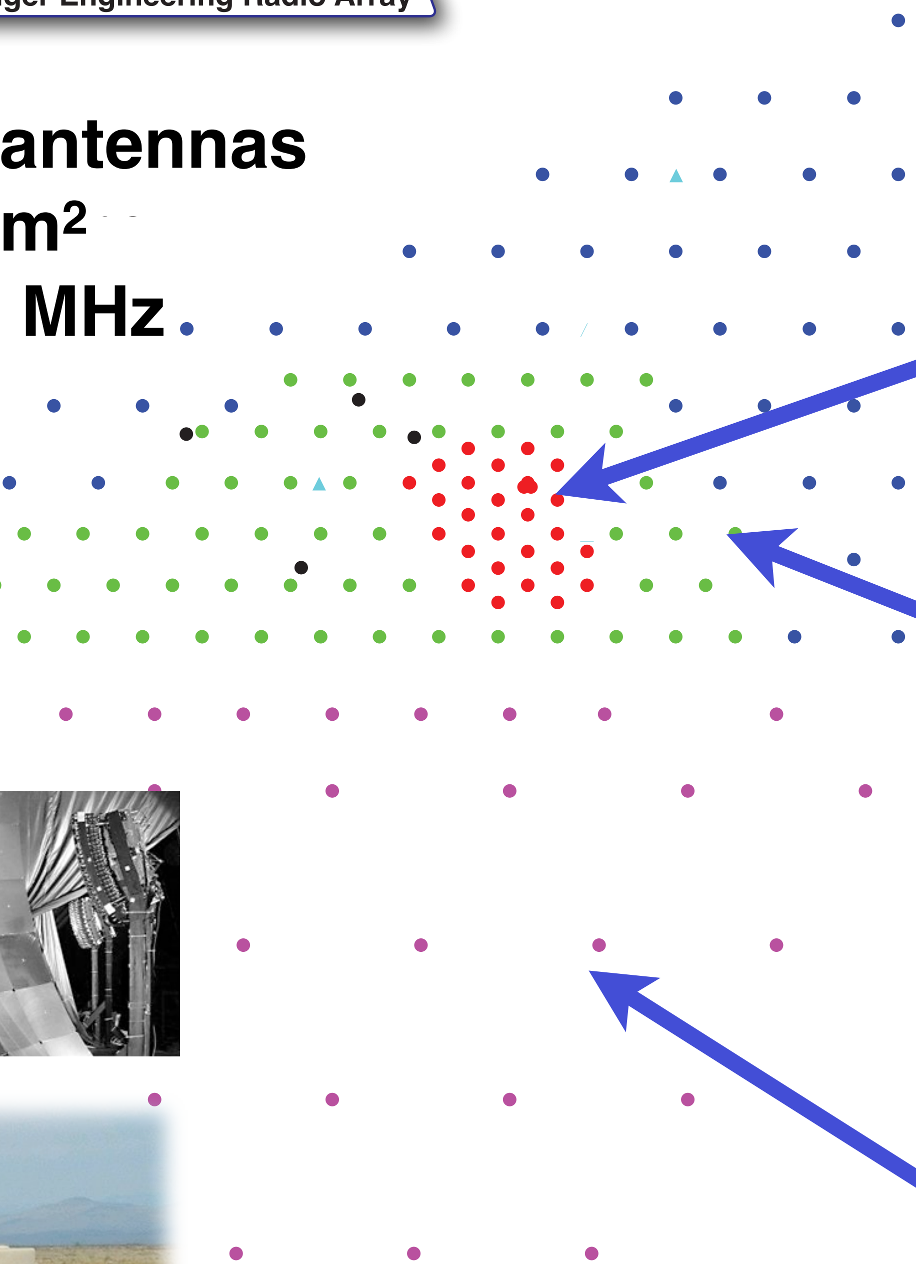

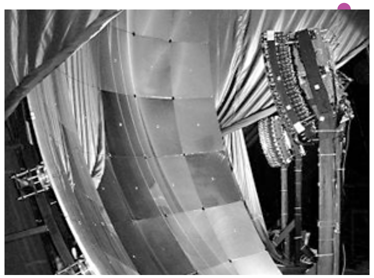

AERA basic idea

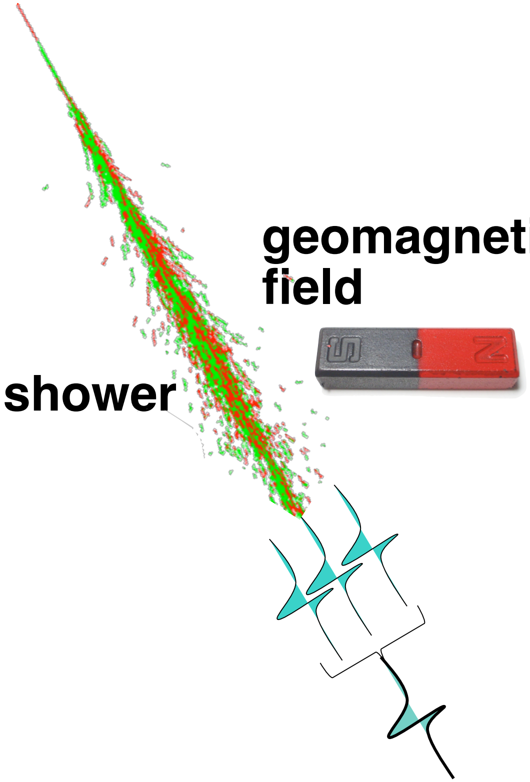

geomagnetic field

air shower

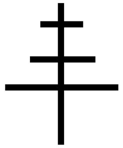

two antenna types:
- LPDA
- butterfly

data taking:
- trigger through SD (CDAS), radio self trigger, int. scint. trigger
- all AERA data are combined in DAQ at Co

DAQ (@CO)
Co comms tower

<-- T2
T3 -->

PIERRE AUGER OBSERVATORY

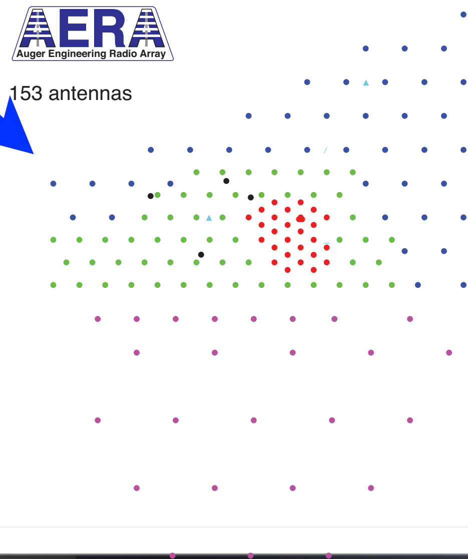

autarcic system:
- solar power
- battery buffer
- GPS -> time
- wireless comms
  (fiber in 1st phase)

measure electric fields in
NS and EW directions
two digitizer types:
- ring buffer + external trigger (SD) (Ger)
- selftrigger + internal scintillator trigger (NL)

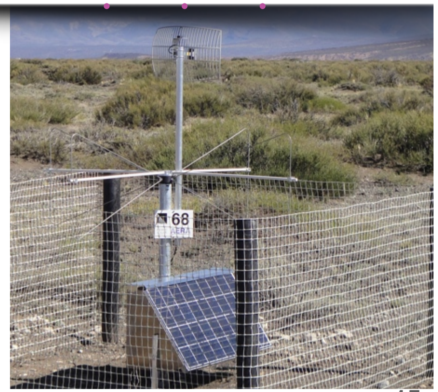

AERA Auger Engineering Radio Array

station layout

24 LPDA

dense core with fiber read-out

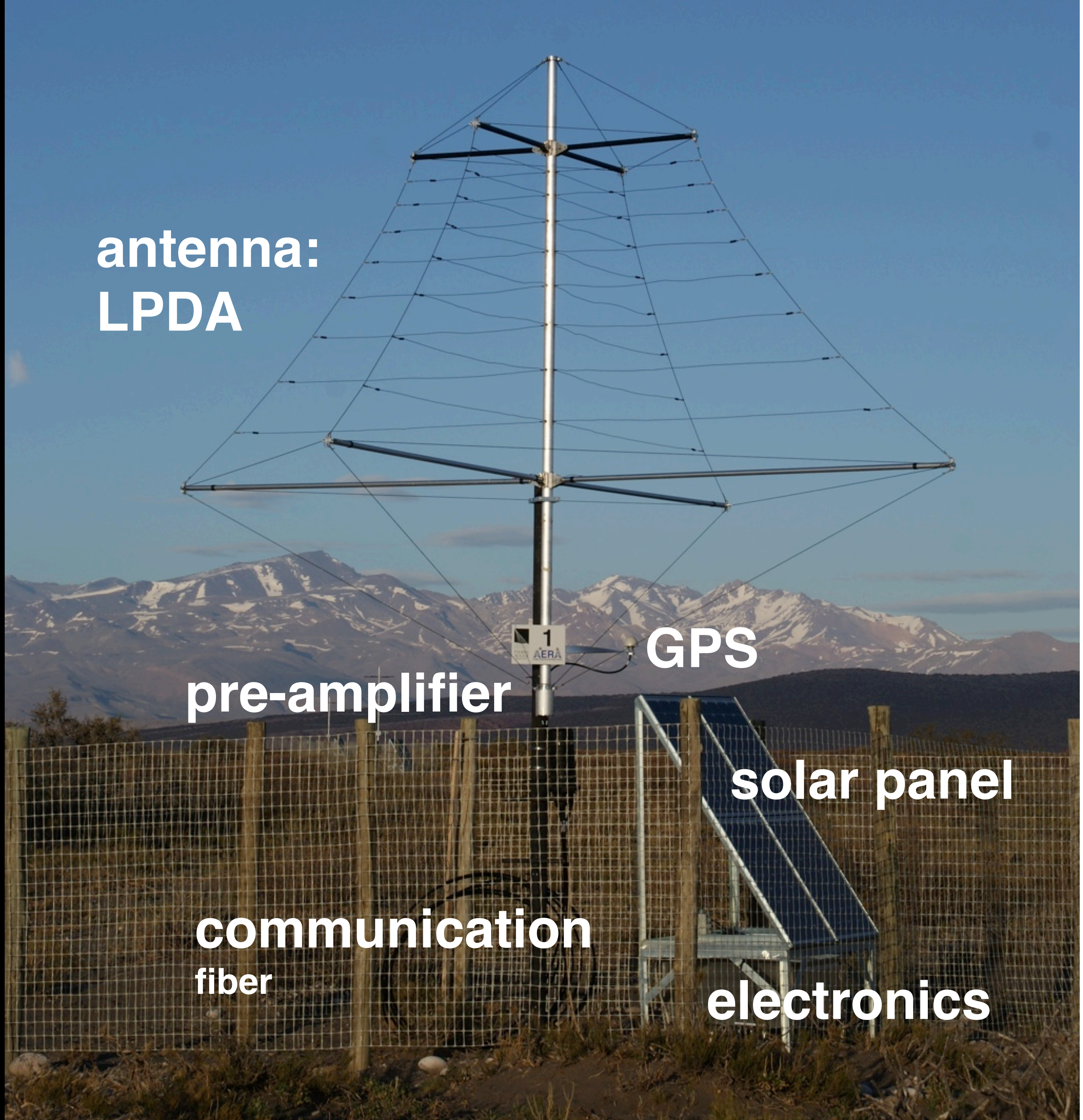

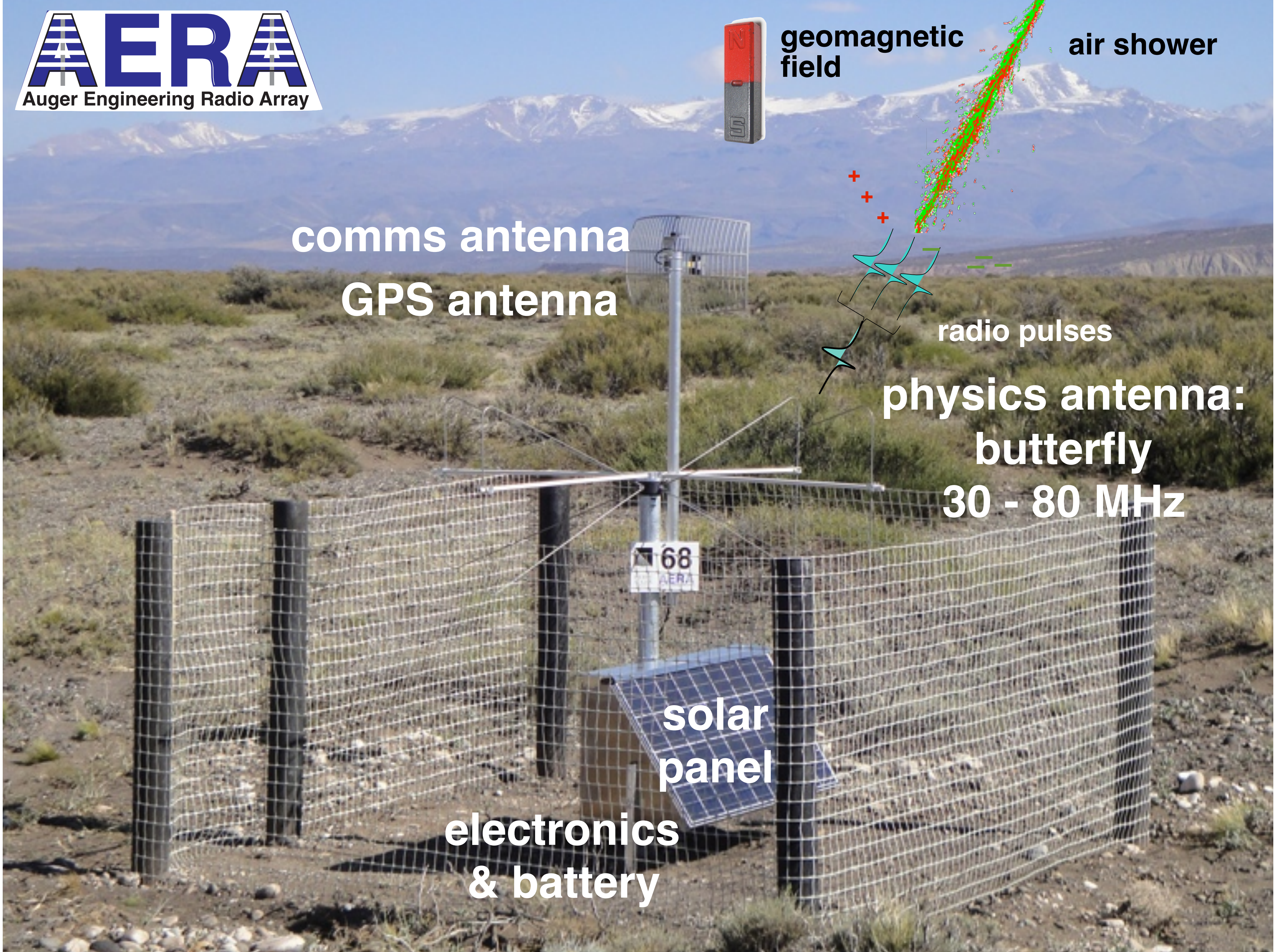
AERA
Auger Engineering Radio Array
N
S
geomagnetic field
air shower
comms antenna
GPS antenna
radio pulses
physics antenna:
butterfly
30 - 80 MHz
68
AERA
solar
panel
electronics
& battery

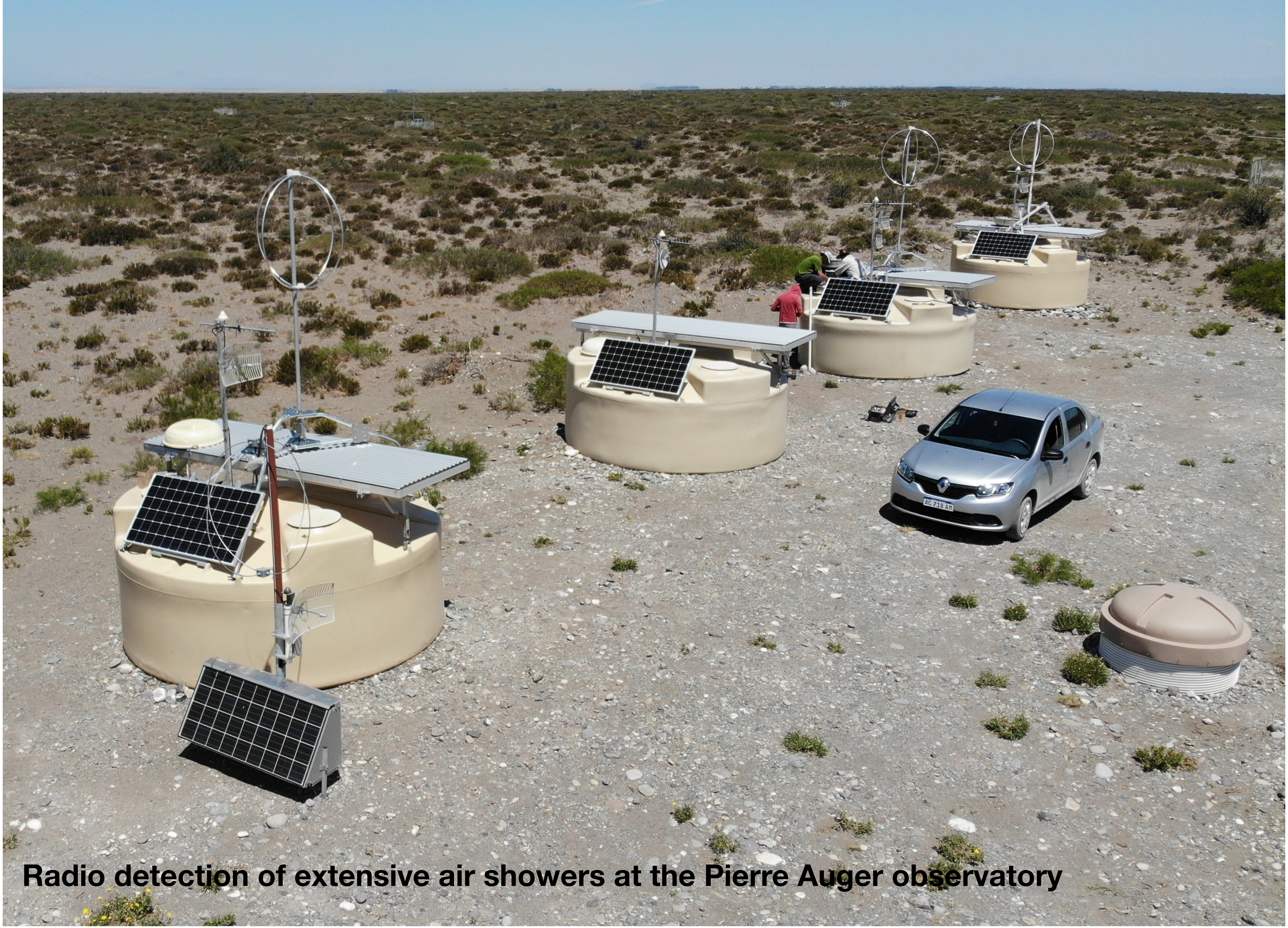

Radio detection of extensive air showers at the Pierre Auger observatory

Calibration

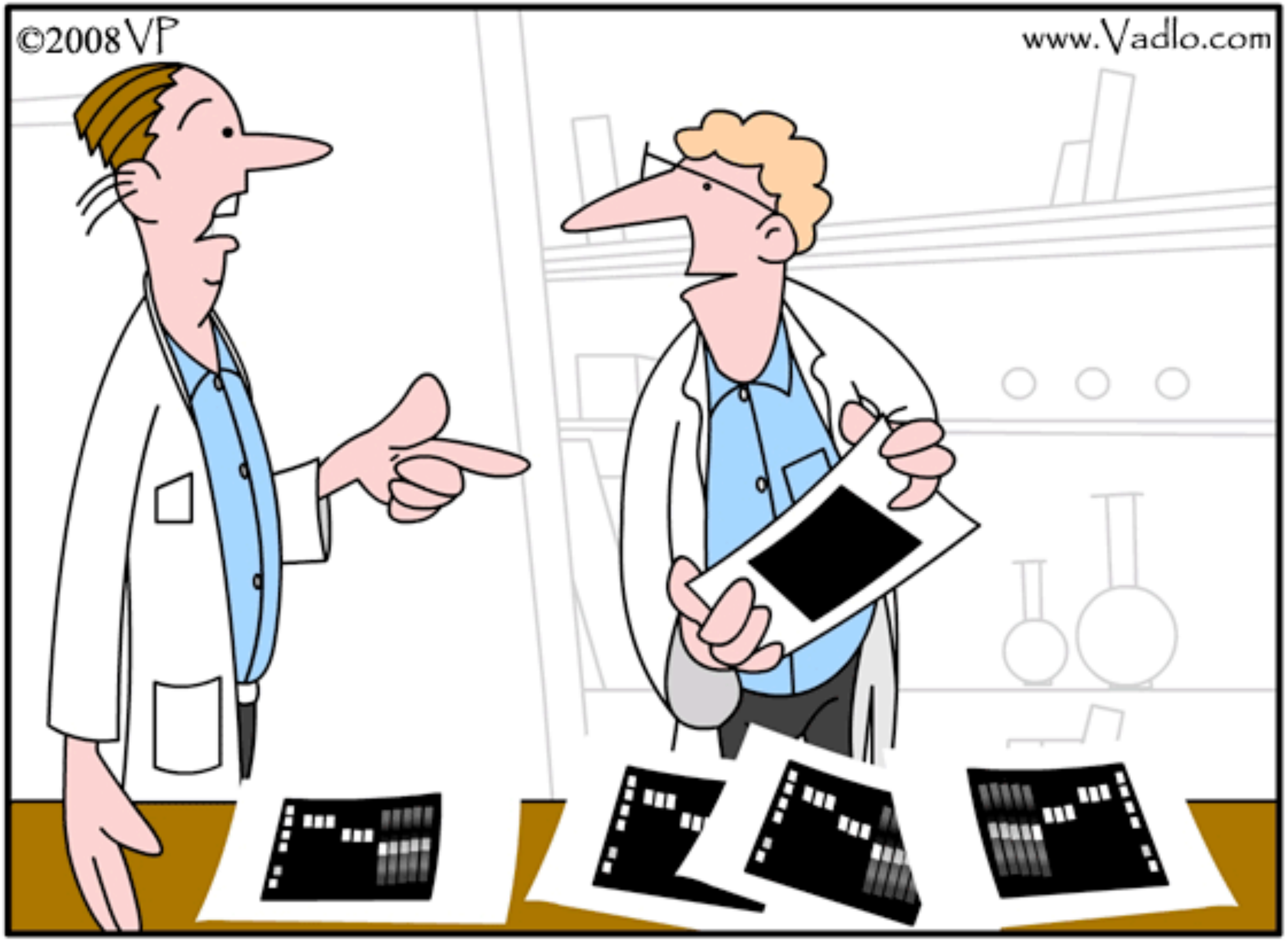

Data don't make any sense, we will have to resort to ***statistics****.*

LOFAR LBA Calibration

measured signal recorded in ADC counts (P_m)

voltage received at the antenna (P_e)

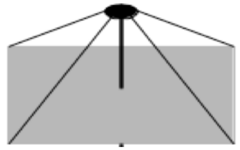

2 independent methods

Nelles, A. et al. 2015, Journal of Instrumentation, 10, P11005

1. Reference Source

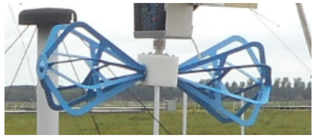

+ Angular response
- Relies on conflicting manufacturer data sheets
- Not easily repeatable

2. Galactic Emission

- Average over whole sky
+ Can be done anytime
- Large error bars due to electronic noise

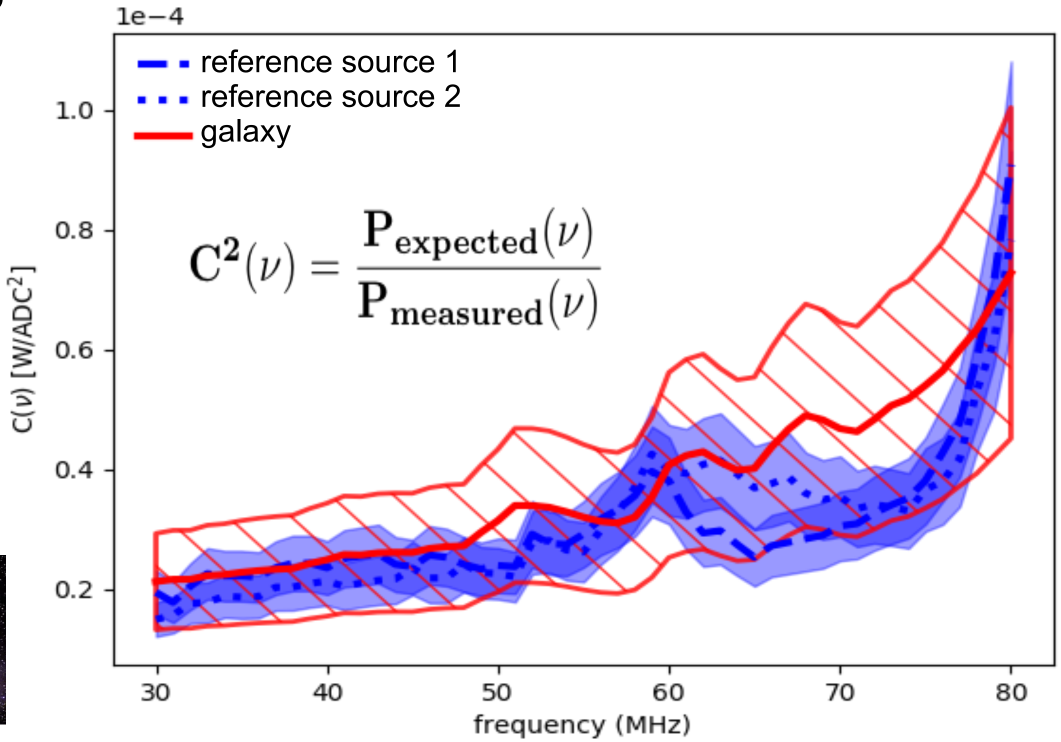

1

Galactic Calibration

LOFAR

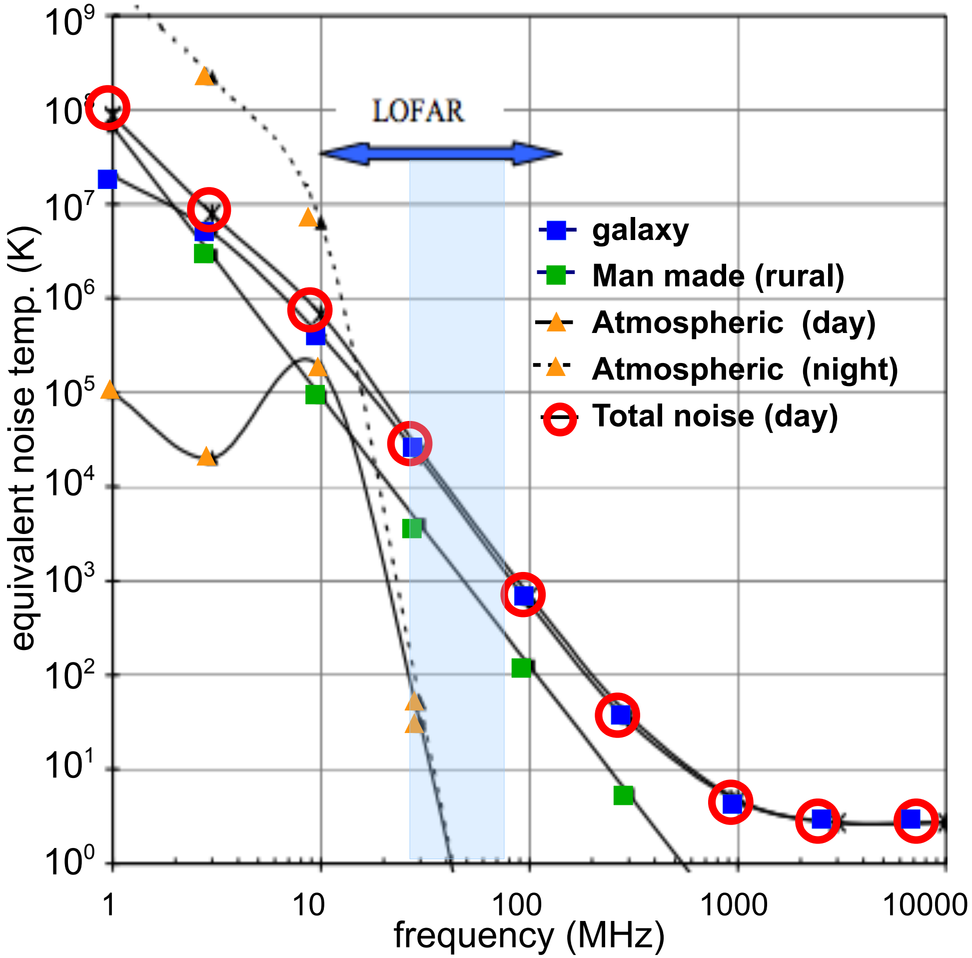

$$C^2(\nu) = \frac{P_{sky+elec.noise}(\nu)}{P_{measured}(\nu)}$$

- Galaxy noise is primary external source of noise in LBA frequency range

  Galaxy noise + electronic noise = recorded signal

- **Lfmap** software provides frequency dependent galactic noise temperature

$$T_{sky}(\nu, \alpha, \delta) = T_{CMB} + T_{Iso}(\nu) + T_{gal}(\nu, \alpha, \delta)$$

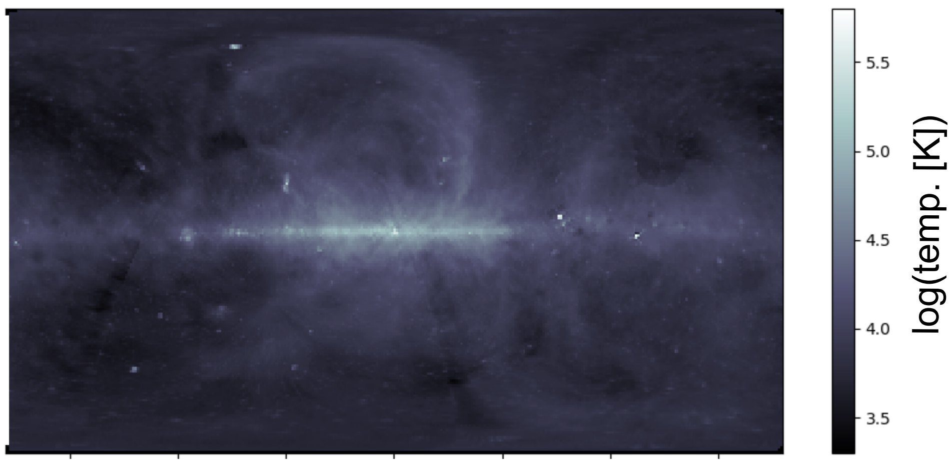

E. Polisensky, LFmap: A Low Frequency Sky Map Generating Program. , Long Wavelength Array (LWA) Memo Series 111 (2007).

3

K. Mulrey, ARENA 2018

Simulating Galaxy Noise

Visible galaxy at 00.00,6:00,12:00,18:00 Local Sidereal Time

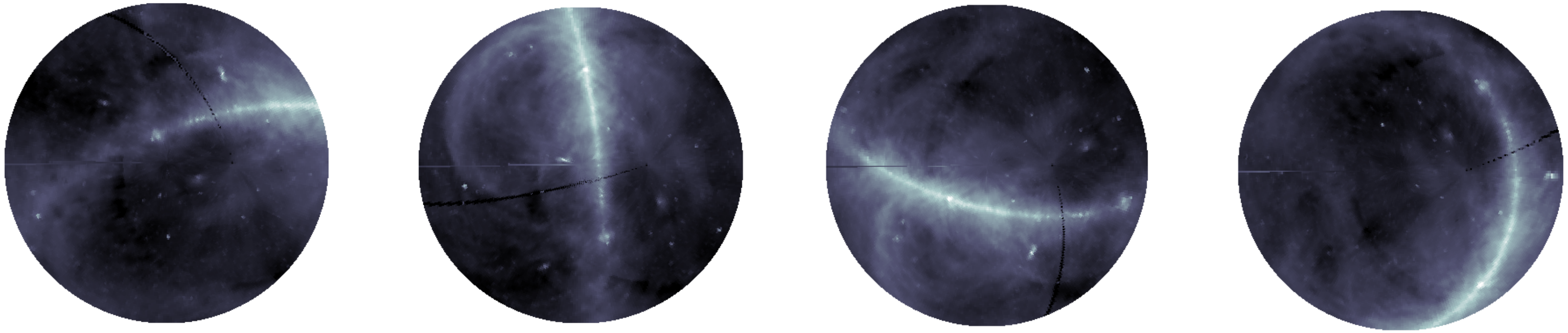

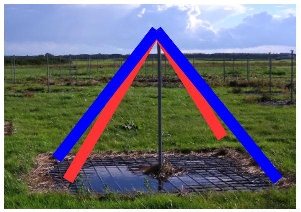

$$\mathrm{P}(\nu) = \frac{2\mathrm{k_B}}{\mathrm{c}^2}\nu^2 \int \mathrm{T_{sky}}(\nu,\theta,\phi)\frac{|\vec{\mathrm{H}}(\nu,\theta,\phi)|^2\mathrm{Z_0}}{2\mathrm{Z_a}}\mathrm{d}\Omega \quad \mathrm{WHz^{-1}}$$

Average antenna response at 55 MHz

$$< |\vec{\mathrm{H}}(\nu,\theta,\phi)|^2 >$$

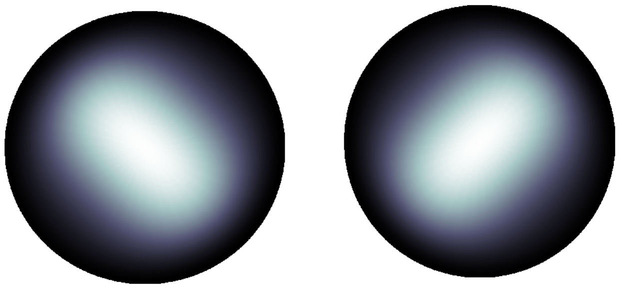

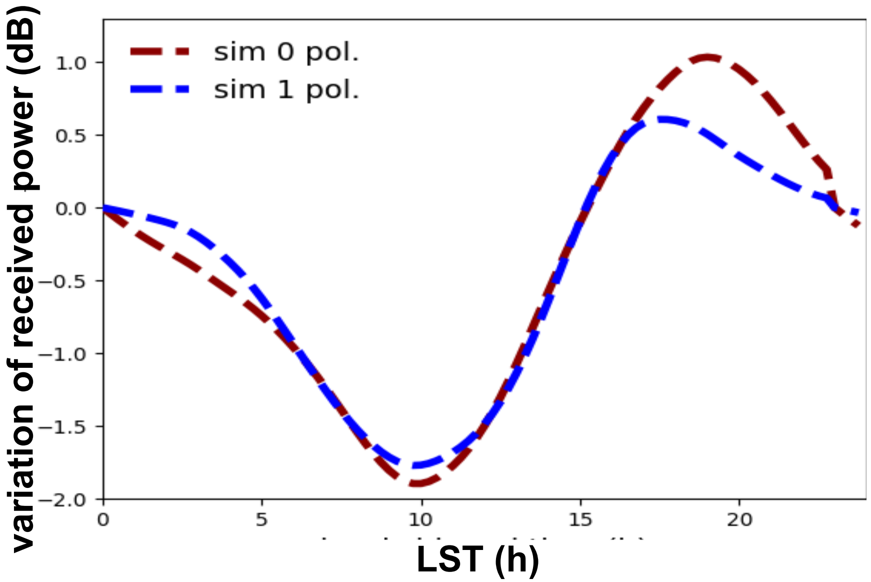

4

K. Mulrey, ARENA 2018

LOFAR Signal Chain

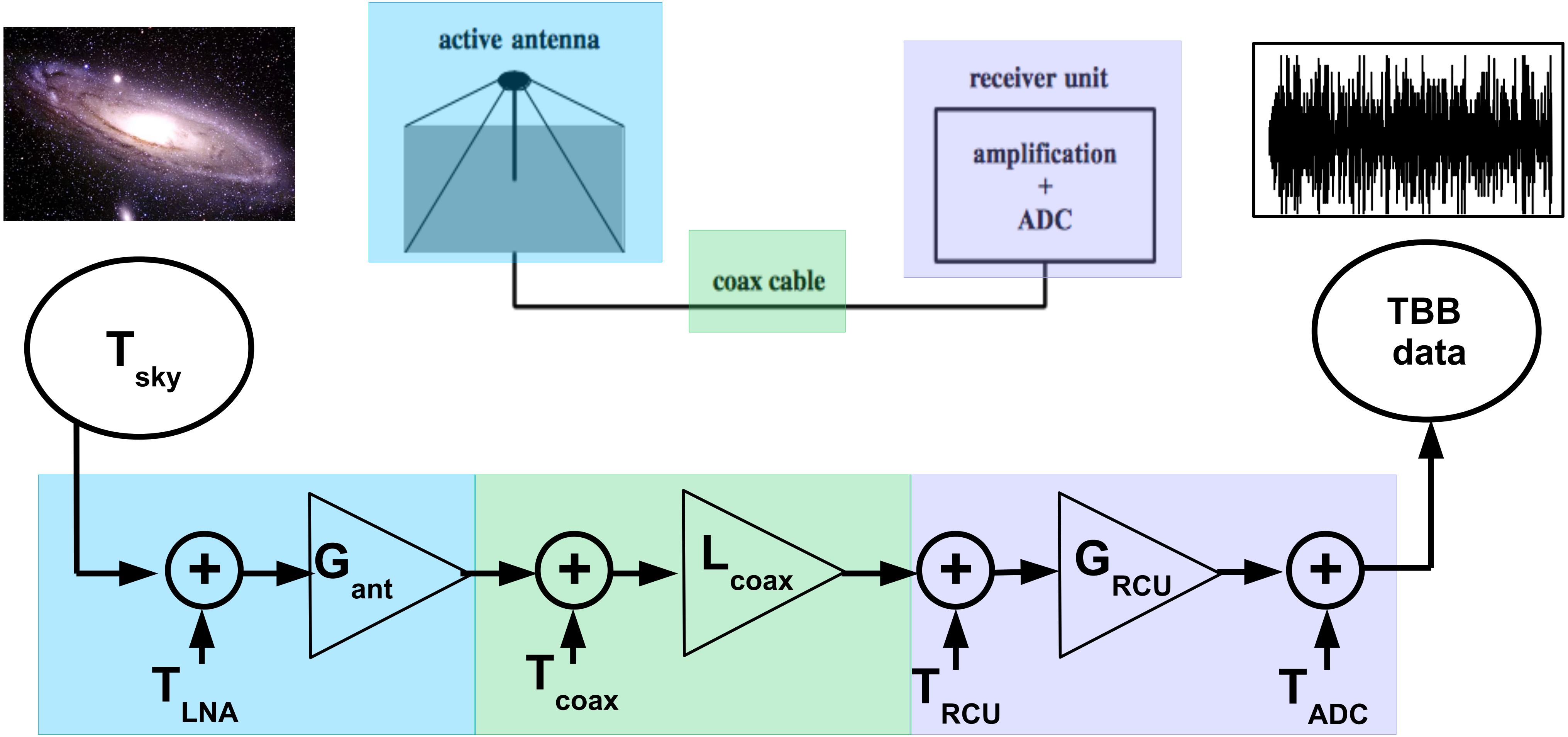

G_{ant} , L_{coax} , G_{RCU} → **Freq. Dependent losses and gains**

T_{LNA} , T_{coax} , T_{RCU} , T_{ADC} → **Constant noise values**

7

K. Mulrey, ARENA 2018

LOFAR Signal Chain

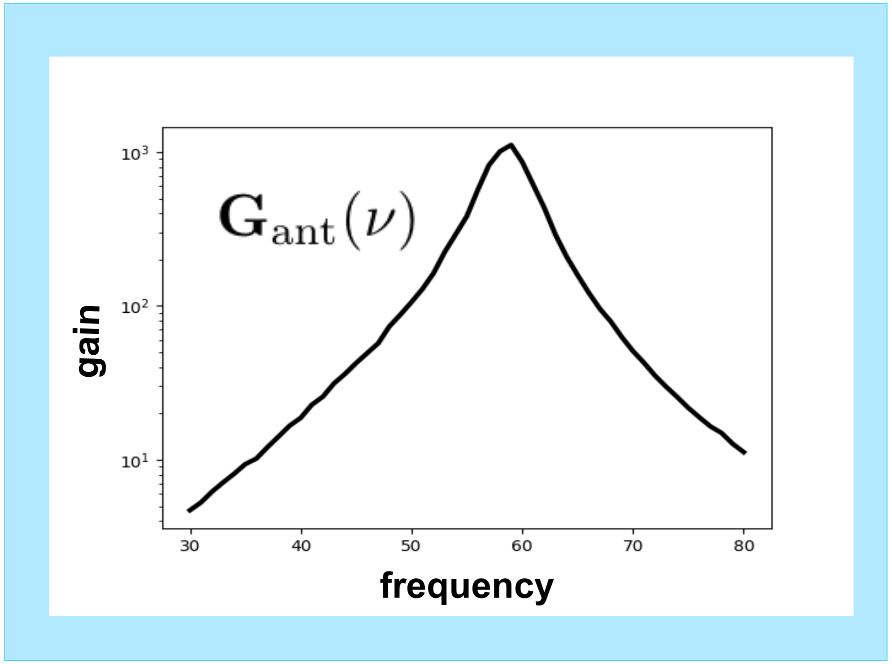

$$\left(\mathbf{P}_{\mathrm{sky}}(\nu, \mathbf{t}) + \mathbf{T}_{\mathrm{LNA}}\right)\mathbf{G}_{\mathrm{ant}}(\nu)\mathbf{A}(\nu)$$

$\mathbf{G}_{\mathrm{ant}}(\nu)$ Antenna gain, simulated with WIPL-D software, with known misaligned resonance frequency

$\mathbf{A}(\nu)$ correction to antenna model

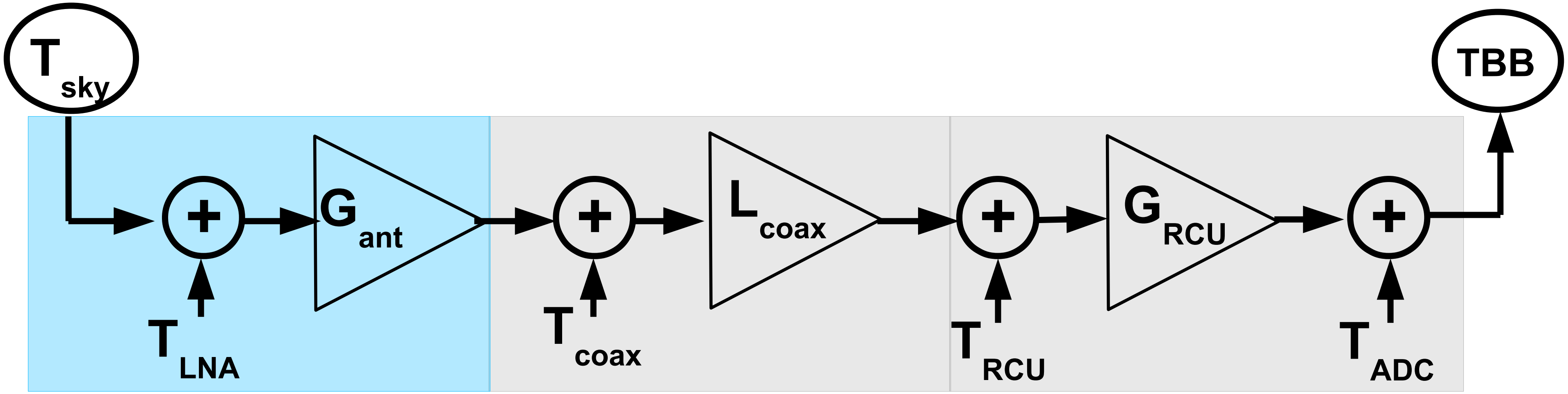

8

K. Mulrey, ARENA 2018

LOFAR Signal Chain

LOFAR

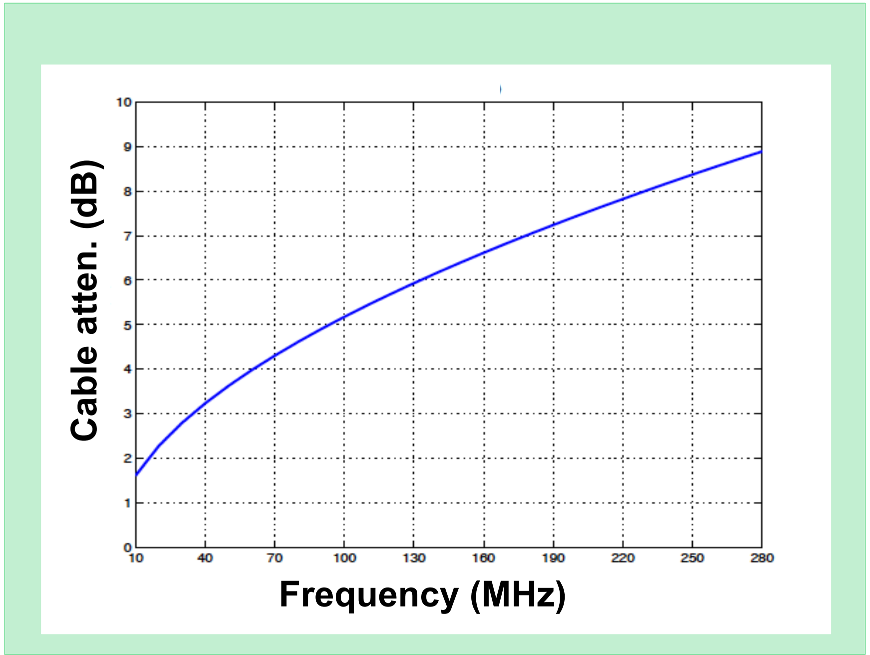

$$\boxed{\left(\mathbf{P}_{\mathrm{sky}}(\nu,\mathbf{t})+\mathbf{T}_{\mathrm{LNA}}\right)\mathbf{G}_{\mathrm{ant}}(\nu)\mathbf{A}(\nu)\mathbf{L}_{\mathrm{coax}}(\nu)}$$

$\mathbf{L}_{\mathrm{coax}}(\nu)$ Cable attenuation (50m, 80m ,115m)

$$\mathbf{T}_{\mathrm{coax}} << \mathbf{T}_{\mathrm{LNA}}, \mathbf{T}_{\mathrm{RCU}}, \mathbf{T}_{\mathrm{ADC}}$$

(not included in model)

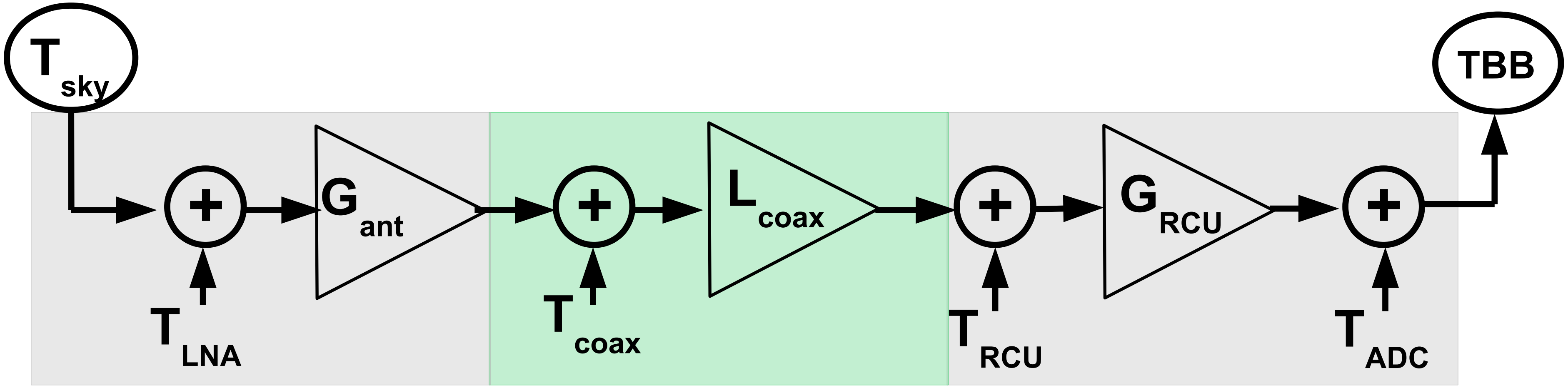

9

K. Mulrey, ARENA 2018

LOFAR Signal Chain

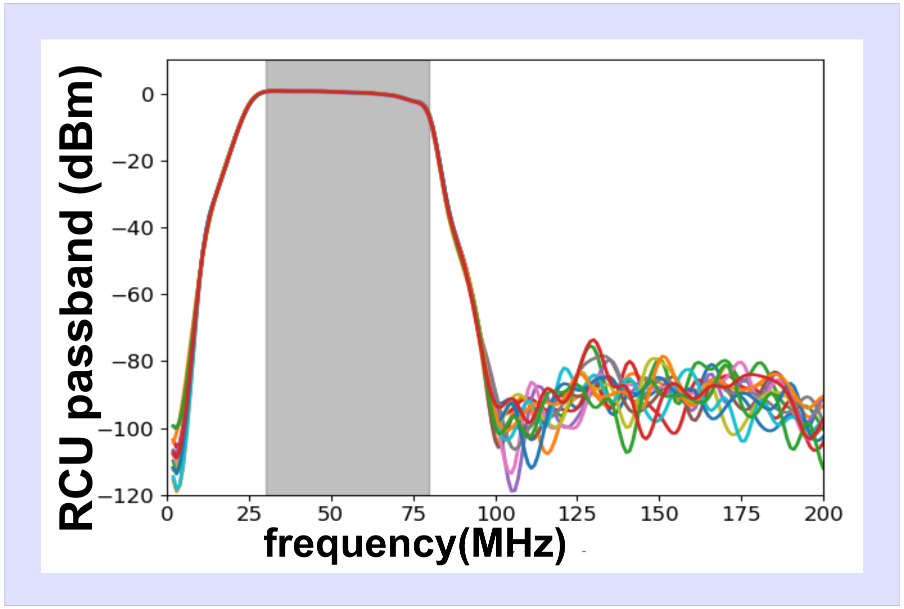

$\mathbf{T}_{\mathrm{RCU}}$ Noise from amplification in RCU

$\mathbf{G}_{\mathrm{RCU}}(\nu)$ RCU passband filter

$\mathbf{S}$ scale factor between voltage and ADC units

$\mathbf{T}_{\mathrm{ADC}}$ time jitter noise from digitization

$$\boxed{\left(\left(\mathbf{P}_{\mathrm{sky}}(\nu,\mathbf{t})+\mathbf{T}_{\mathrm{LNA}}\right)\mathbf{G}_{\mathrm{ant}}(\nu)\mathbf{A}(\nu)\mathbf{L}_{\mathrm{coax}}(\nu)+\mathbf{T}_{\mathrm{RCU}}\right)\mathbf{G}_{\mathrm{RCU}}(\nu)\mathbf{S}+\mathbf{T}_{\mathrm{ADC}}=\mathbf{P}_{\mathrm{sim}}(\nu,\mathbf{t})}$$

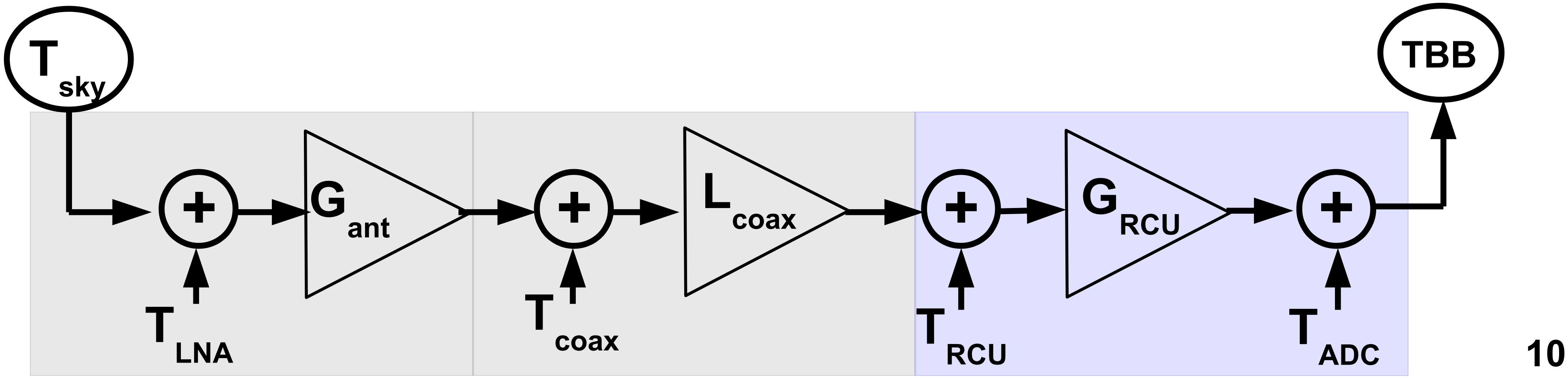

K. Mulrey, ARENA 2018

LOFAR Signal Chain

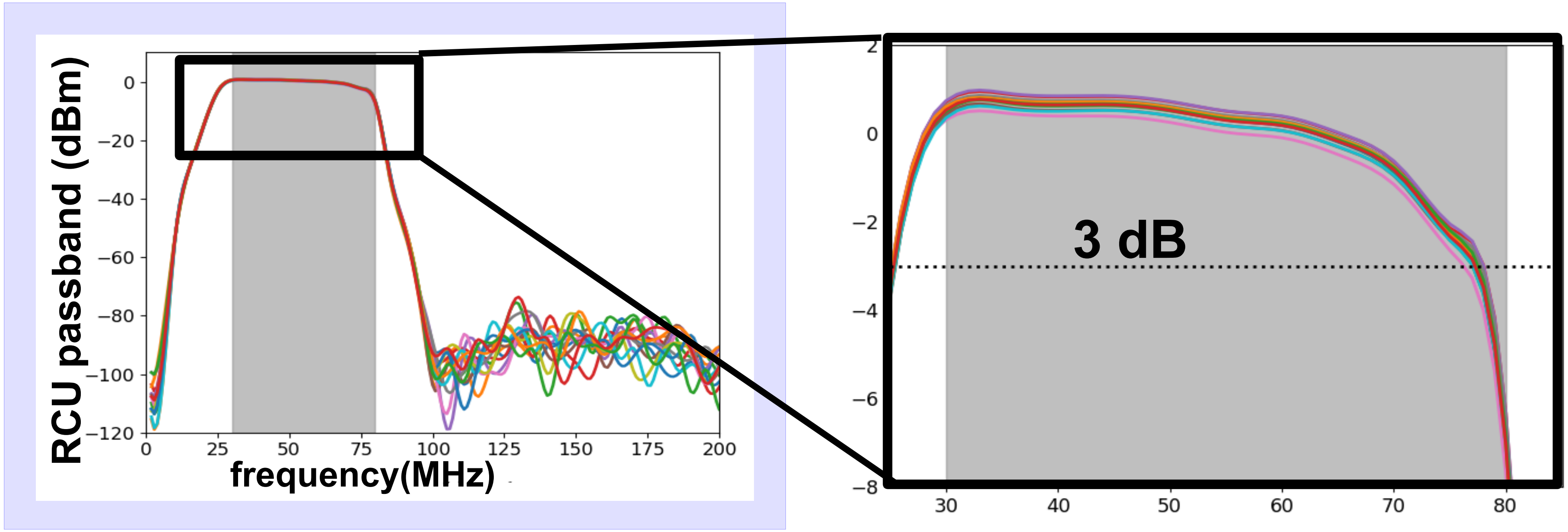

$$\left(\left(\mathbf{P}_{\mathrm{sky}}(\nu,\mathbf{t})+\mathbf{T}_{\mathrm{LNA}}\right)\mathbf{G}_{\mathrm{ant}}(\nu)\mathbf{A}(\nu)\mathbf{L}_{\mathrm{coax}}(\nu)+\mathbf{T}_{\mathrm{RCU}}\right)\mathbf{G}_{\mathrm{RCU}}(\nu)\mathbf{S}+\mathbf{T}_{\mathrm{ADC}}=\mathbf{P}_{\mathrm{sim}}(\nu,\mathbf{t})$$

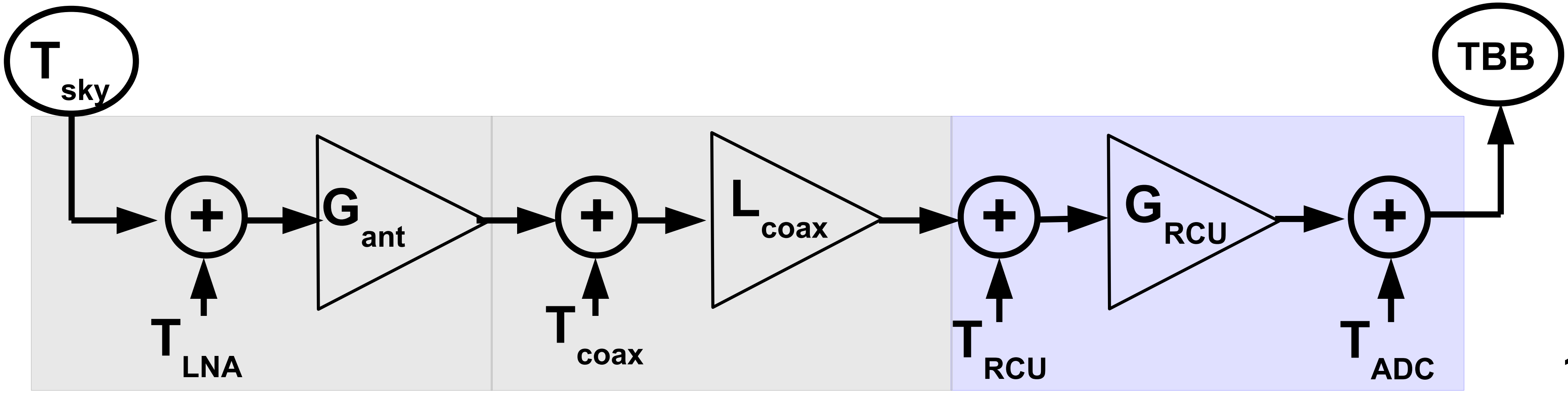

10

K. Mulrey, ARENA 2018

Fitting for Electronic Noise

LOFAR

$$\Big(\big(\mathbf{P}_{\rm sky}(\nu,\mathbf{t}) + \mathbf{T}_{\rm LNA}\big)\mathbf{G}_{\rm ant}(\nu)\mathbf{A}(\nu)\mathbf{L}_{\rm coax}(\nu) + \mathbf{T}_{\rm RCU}\Big)\mathbf{G}_{\rm RCU}(\nu)\mathbf{S} + \mathbf{T}_{\rm ADC} = \mathbf{P}_{\rm sim}(\nu,\mathbf{t})$$

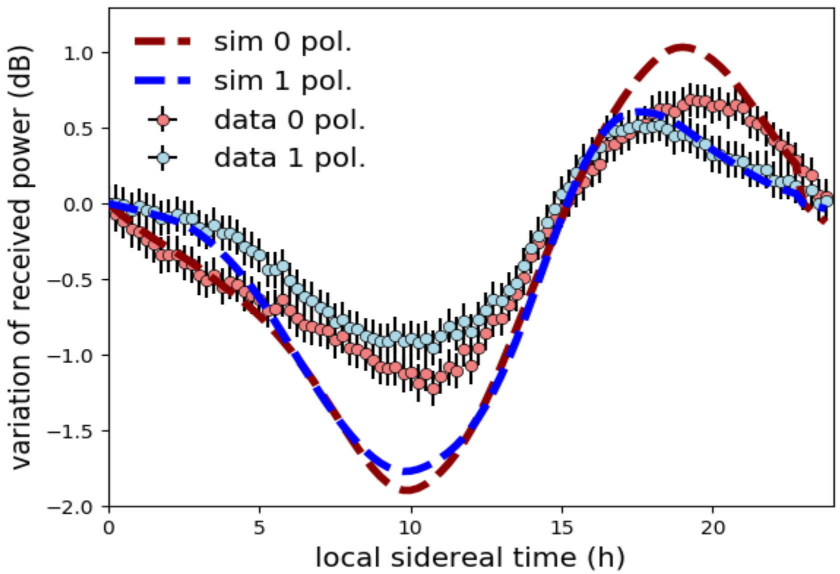

known, frequency dependent quantity

unknown, constant quantity

Fitted noise values at ADC

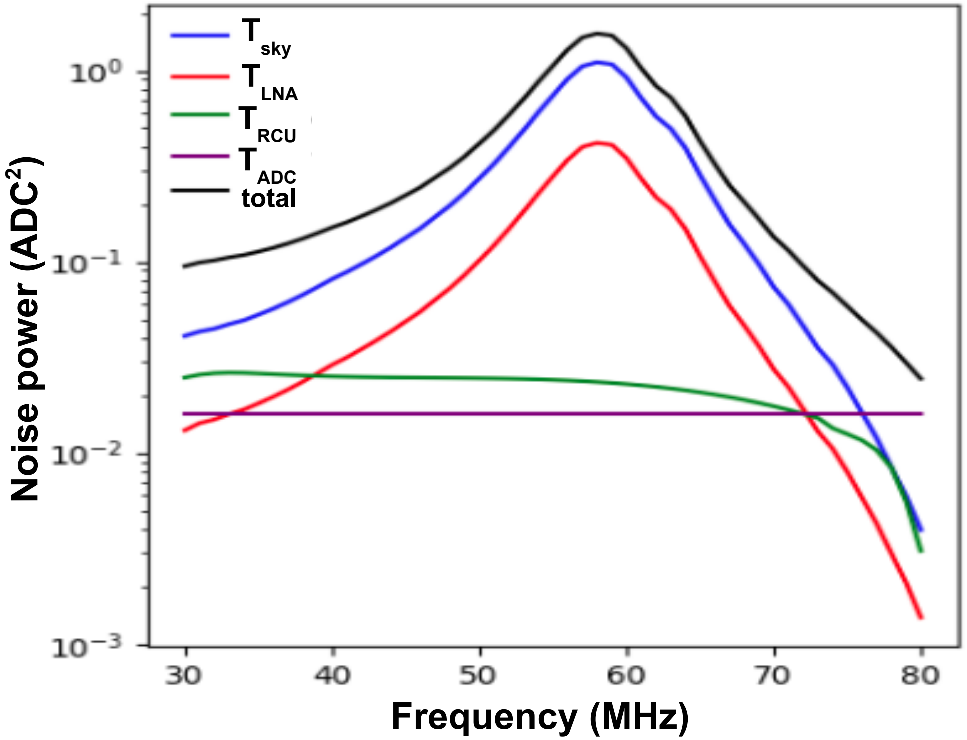

$$X^2 = \sum \frac{(\mathrm{P}(\nu,\mathrm{t})_{\rm data} - \mathrm{P}(\nu,\mathrm{t})_{\rm sim})^2}{\sigma(\nu,\mathrm{t})_{\rm data}}$$

★ All noise contributions are required to fit simulation to data at all frequencies

11

K. Mulrey, ARENA 2018

Calibration Results

$$\mathbf{C^2}(\nu) = \mathbf{A}(\nu)\mathbf{L}_{\text{coax}}(\nu)\mathbf{G}_{\text{RCU}}(\nu)\mathbf{S}$$

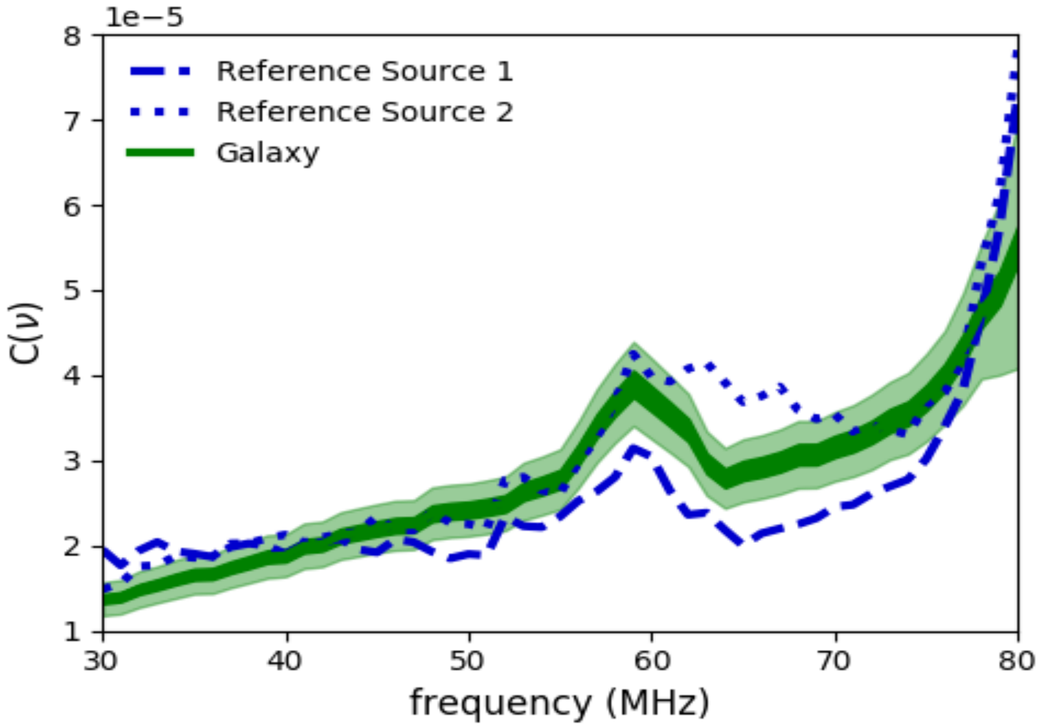

Uncertainty	Percentage
event-to-event fluctuation	4
galaxy model	12
electronic noise $<$ 77 MHz	5-6
electronic noise $>$ 77 MHz	10-20
total $<$ 77 MHz	**14**

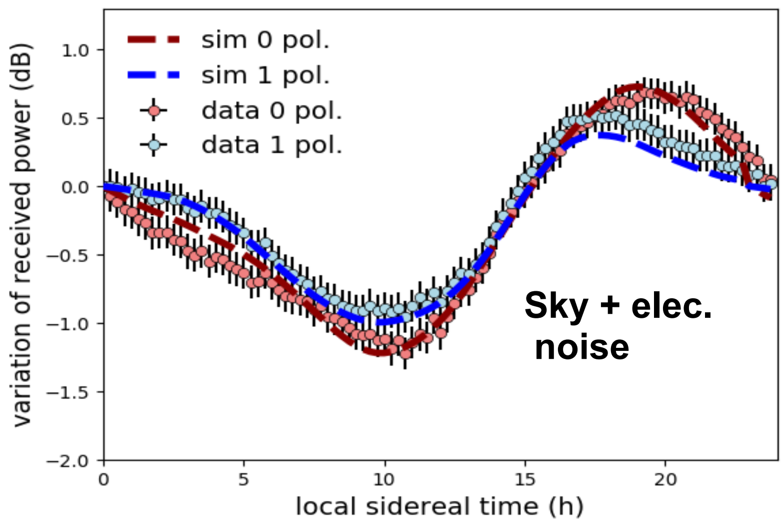

- Galaxy model now limits systematic uncertainties
- Uncertainties from electronic noise are found by comparing resulting calibration constants for different antennas

12

K. Mulrey, ARENA 2018

Comparison to CoREAS

For ~20 strong events (x 3 stations x 48 antennas), compare slope on either side of resonance frequency

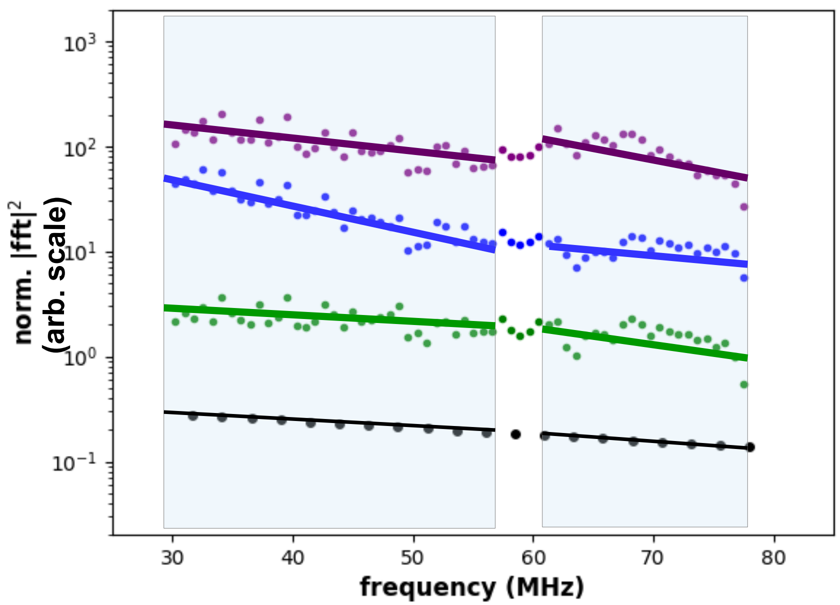

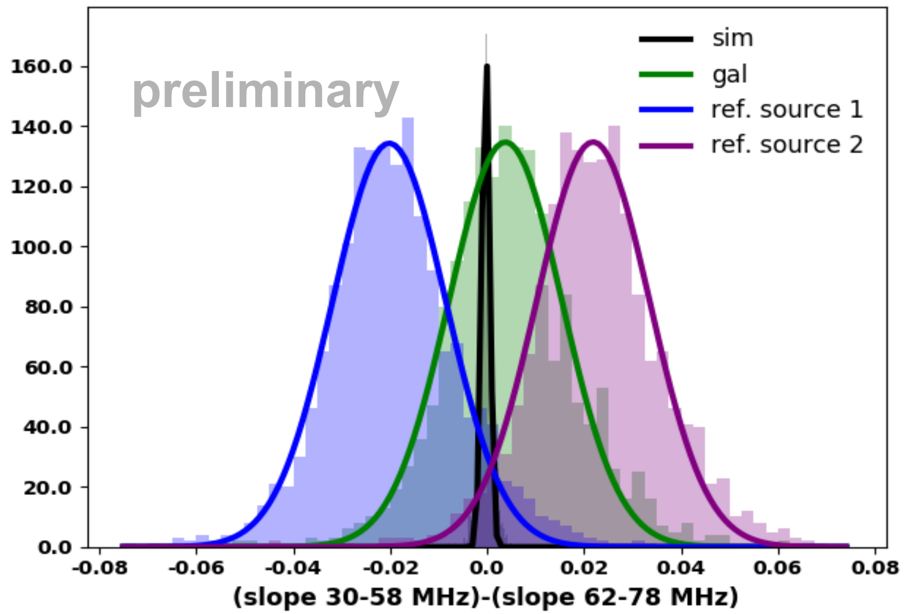

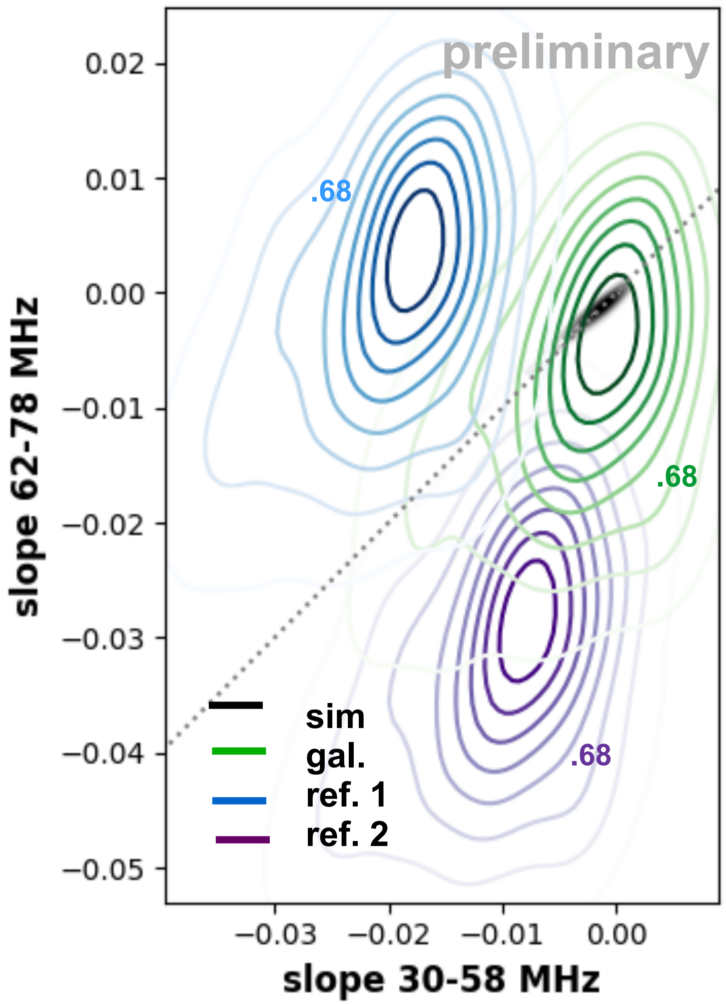

13

Timing calibration

Use beacon broadcasting at 4 different frequencies to measure relative time shifts

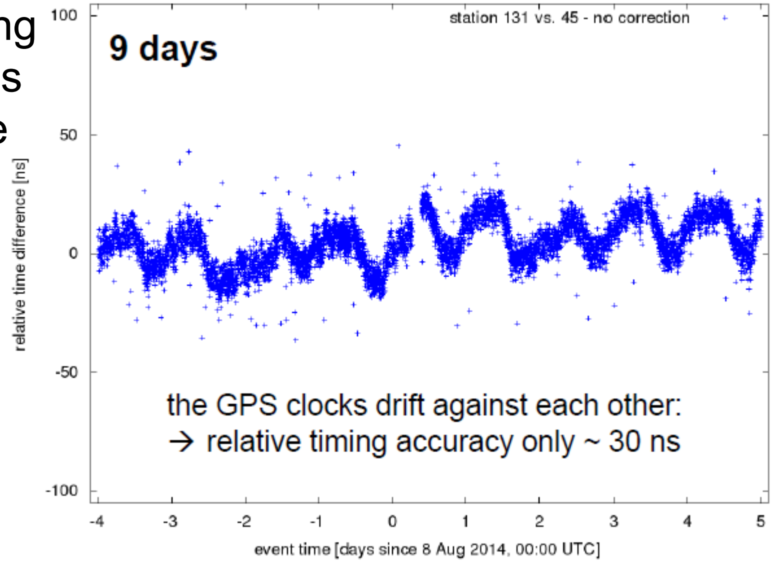

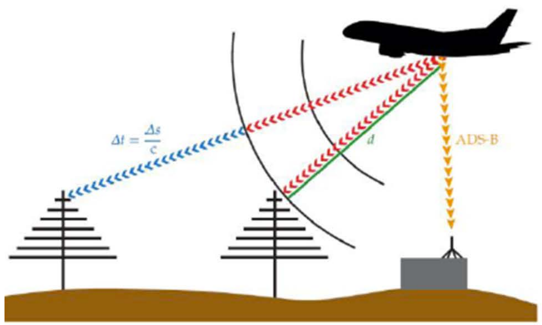

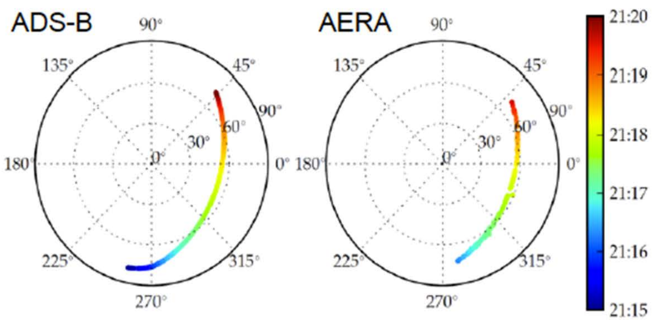

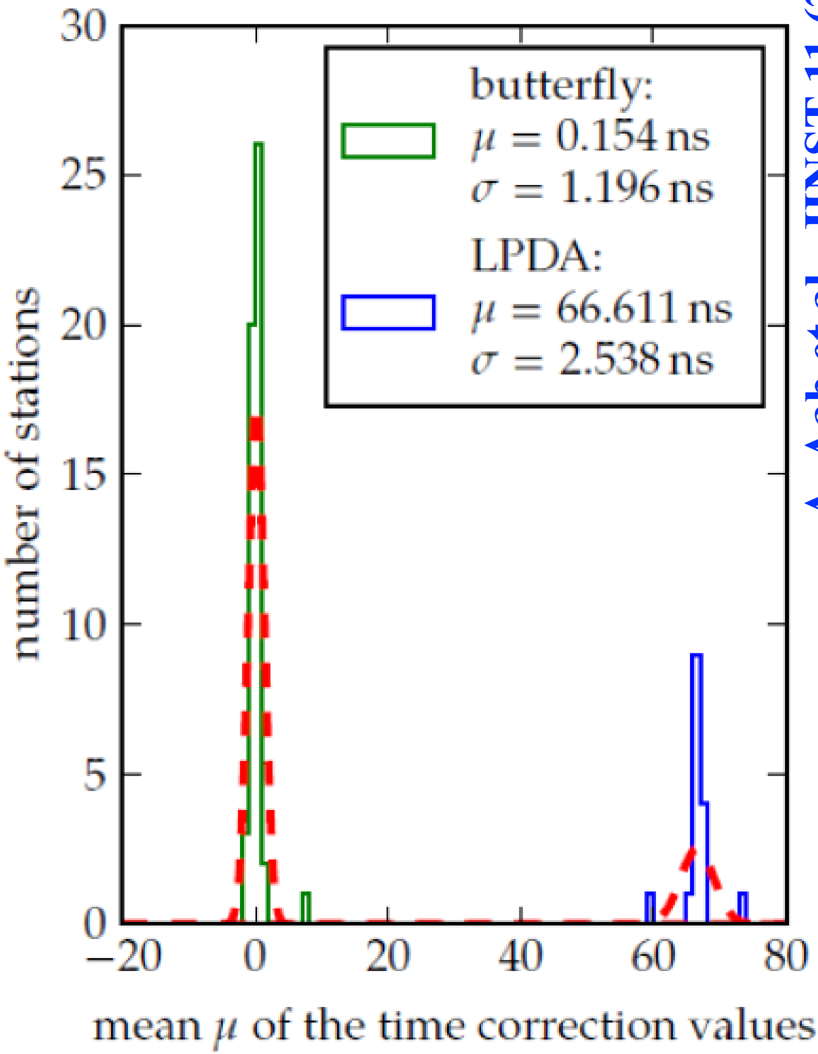

A. Aab et al., JINST 11 (2016) no.01, P01018

Scintillation detectors are frequently used to detect charged particles

charged particles deposit energy in a material through ionization losses

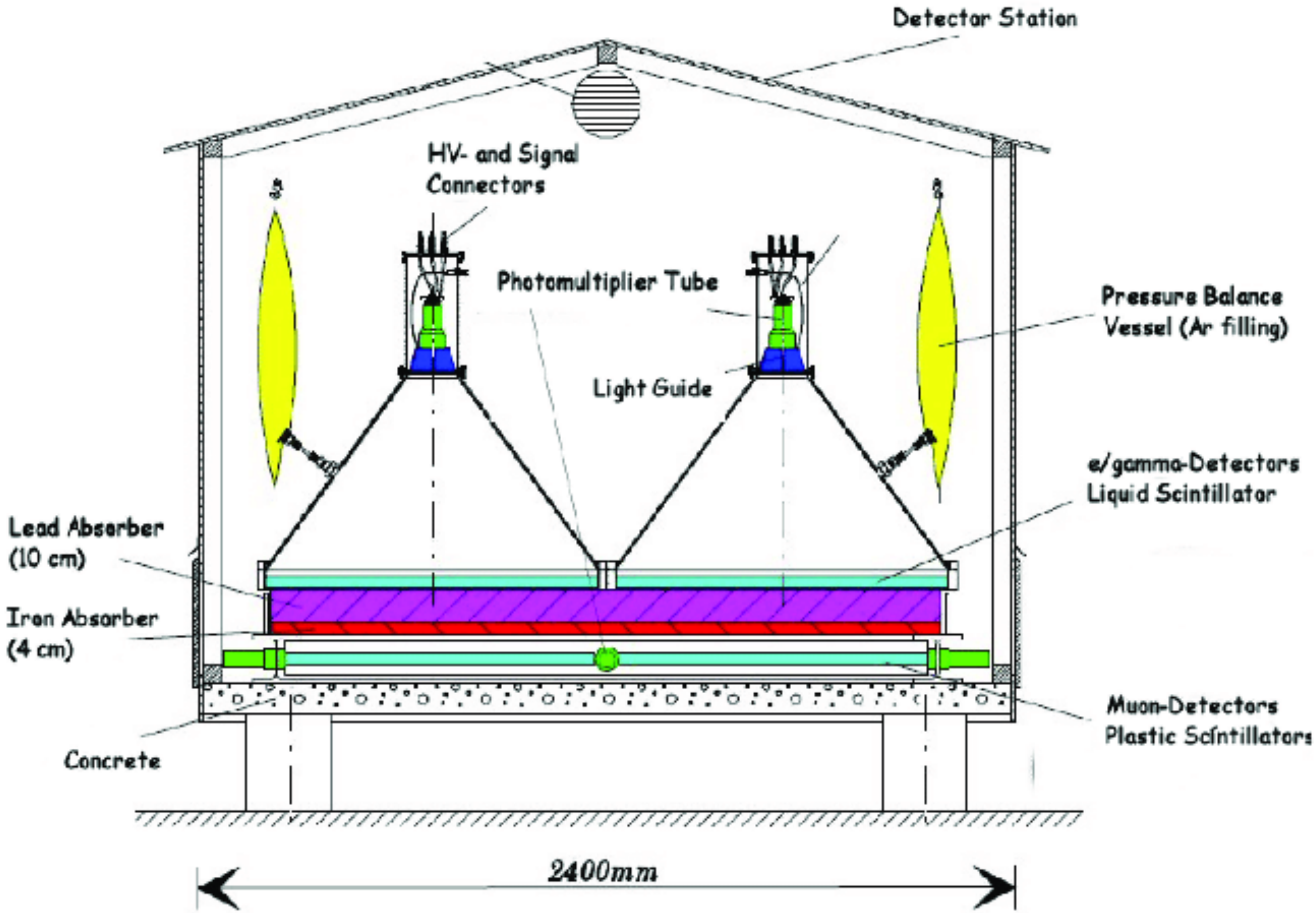

Ionization loss

charged particles traveling through matter lose energy on excitation and ionization of its atoms

energy loss per unit of column depth [MeV per g/cm²]

Bethe-Bloch equation

$$\frac{dE}{dx} = -\frac{N_A Z}{A}\frac{2\pi(ze^2)^2}{Mv^2}\left[\ln\frac{2Mv^2\gamma^2W}{I^2} - 2\beta^2\right]$$

I **average ionization potential**

W **maximum energy loss**

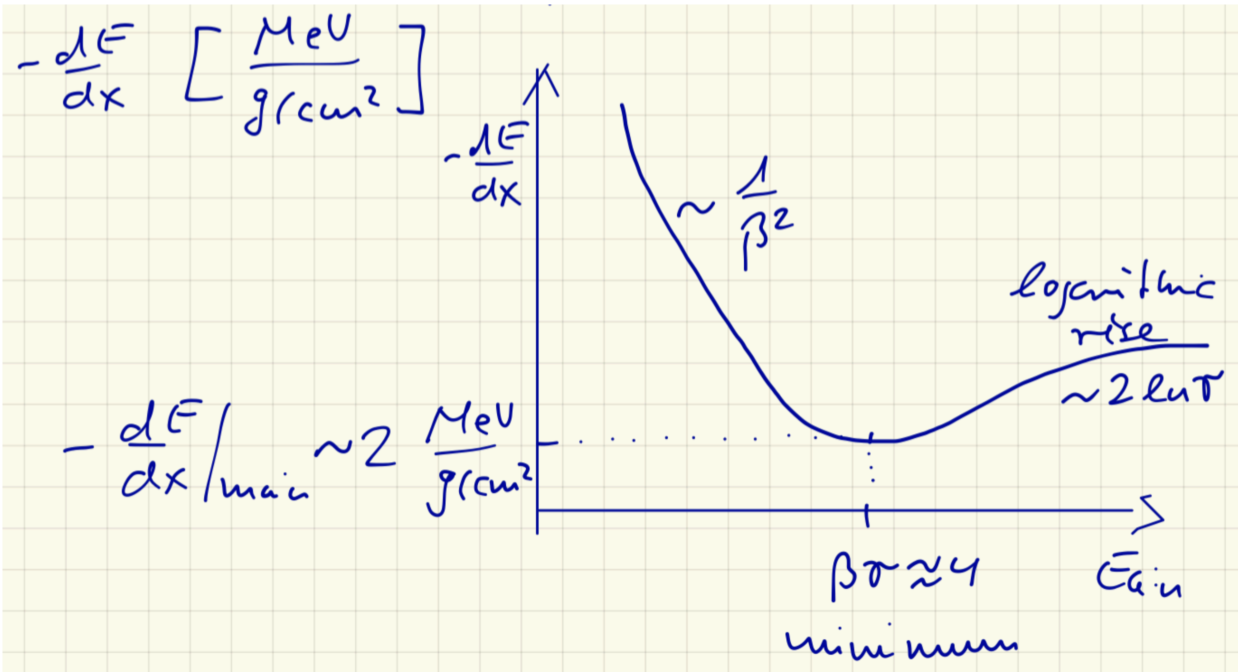

the ionization loss is proportional to a constant L that includes the charge and atomic number fo the medium

$$L = \frac{2\pi N_A Z}{A} \left(\frac{e^2}{mc^2} \right)^2 mc^2 = 0.0765 \left(\frac{2Z}{A} \right) \quad \text{MeV/(g cm}^2\text{)}$$

for dense media: reduction of logarithmic rise (density effect)

$$\frac{dE}{dx} = -L \frac{Z^2}{\beta^2} \left(B + 0.69 + 2 \ln \gamma\beta + \ln W - 2\beta^2 - \delta \right) \quad \text{MeV/(g cm}^2\text{)}$$

$$B = \ln \left(\frac{mc^2}{I} \right) \qquad W \approx \frac{E}{2}$$

$$\delta = 2 \ln \gamma\beta + C$$

C **correction factor (Sternheimer)**

element	I, eV	L	B	C
hydrogen	21.8	152	21.07	-9.50
helium	44.0	77	19.39	-2.13
carbon	77.8	77	18.25	-3.22
nitrogen	90.0	77	17.67	-10.68
oxygen	104	77	17.67	-10.80
iron	286	72	15.32	-4.62

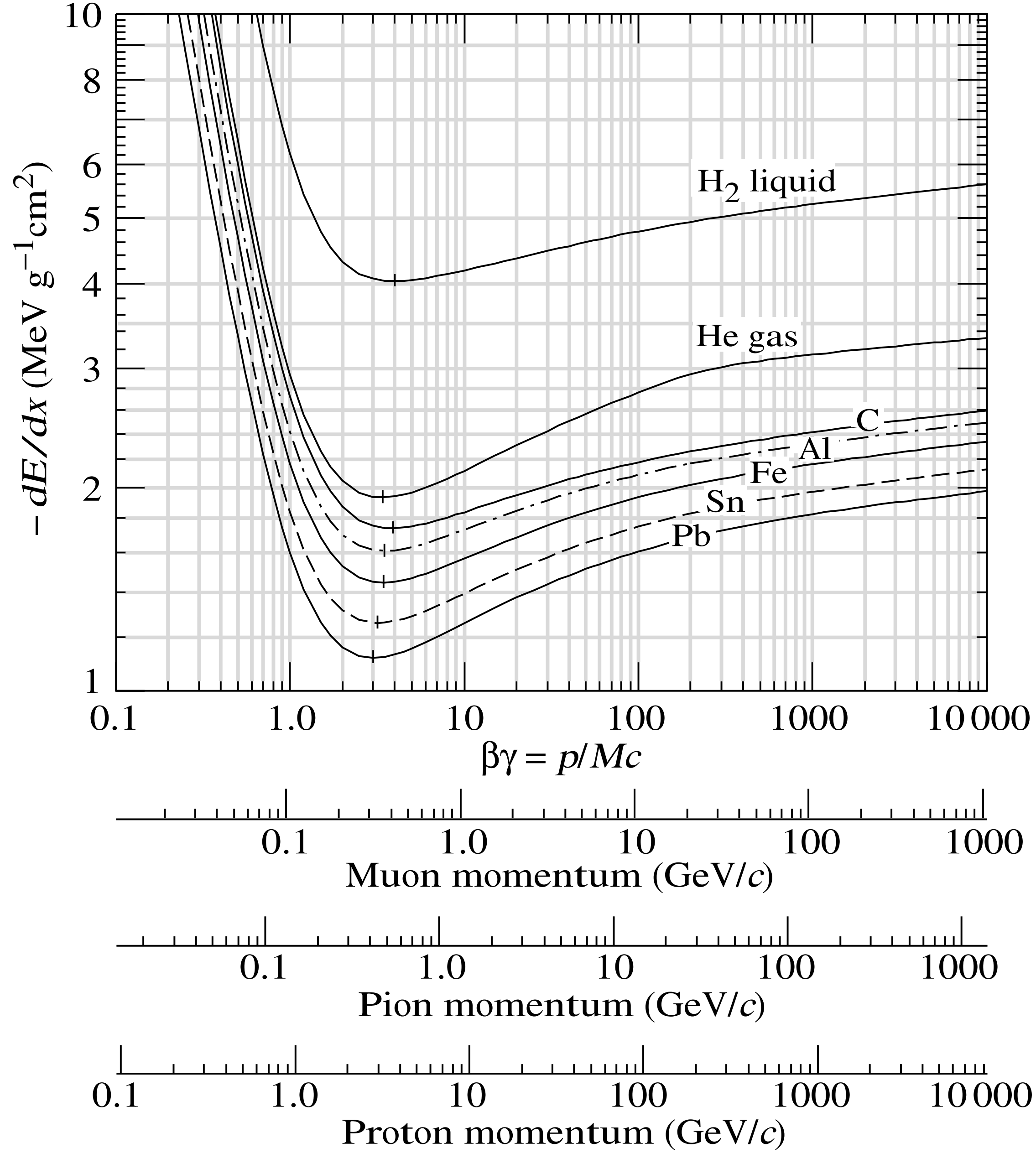

Figure 27.2: Mean energy loss rate in liquid (bubble chamber) hydrogen, gaseous helium, carbon, aluminum, iron, tin, and lead. Radiative effects, relevant for muons and pions, are not included. These become significant for muons in iron for $\beta\gamma \gtrsim 1000$, and at lower momenta for muons in higher-Z absorbers. See Fig. 27.21.

Scintillation Detectors

Particle Detection via Luminescence

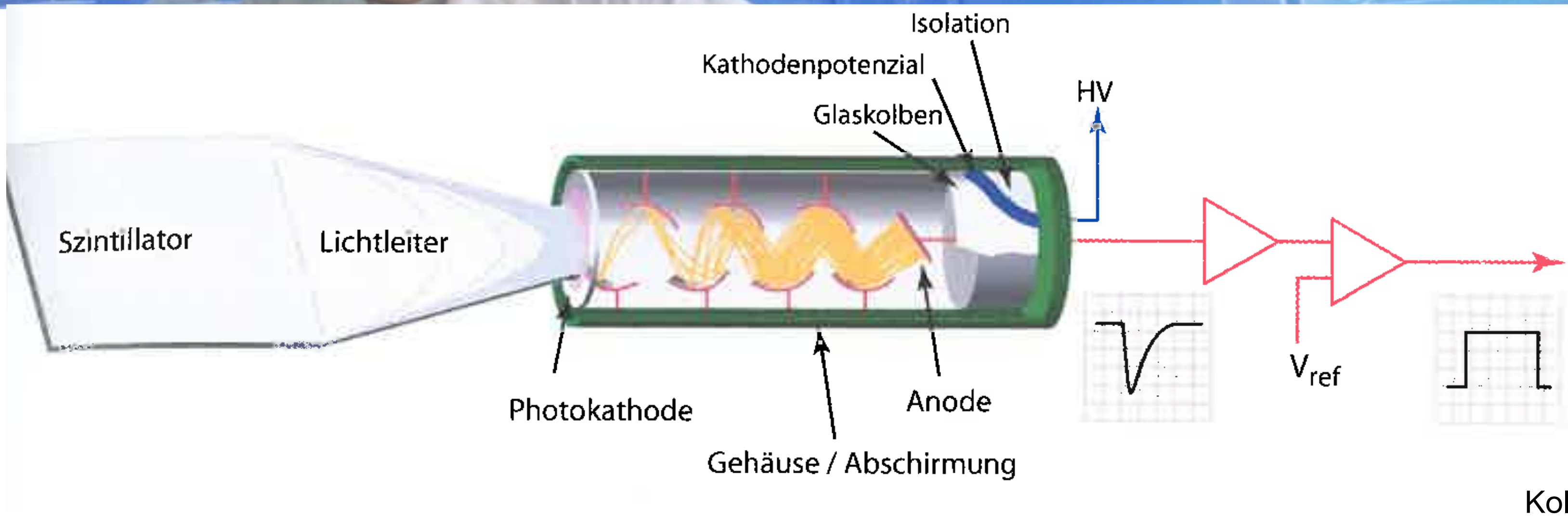

Kolanoski, Wermes

Scintillators – General Characteristics

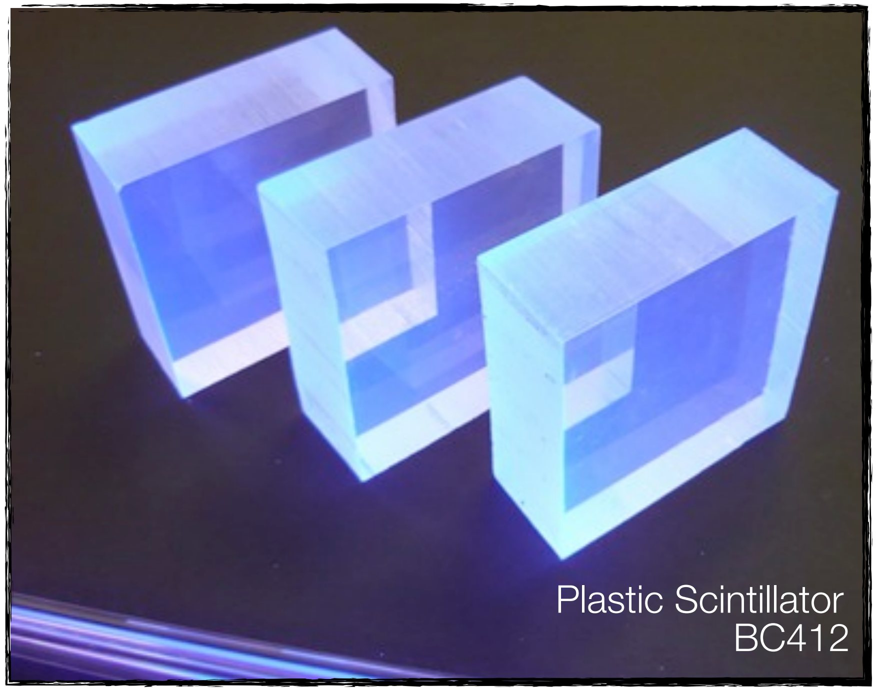

Principle:

dE/dx converted into visible light
Detection via photosensor
[e.g. photomultiplier, human eye ...]

Main Features:

Sensitivity to energy
Fast time response
Pulse shape discrimination

Requirements

High efficiency for conversion of exciting energy to fluorescent radiation
Transparency to its fluorescent radiation to allow transmission of light
Emission of light in a spectral range detectable for photosensors
Short decay time to allow fast response

Inorganic Crystals

Materials:

Sodium iodide (NaI)
Cesium iodide (CsI)
Barium fluoride (BaF_2)
...

Mechanism:

Energy deposition by ionization
Energy transfer to impurities
Radiation of scintillation photons

Time constants:

Fast: recombination from activation centers [ns ... µs]
Slow: recombination due to trapping [ms ... s]

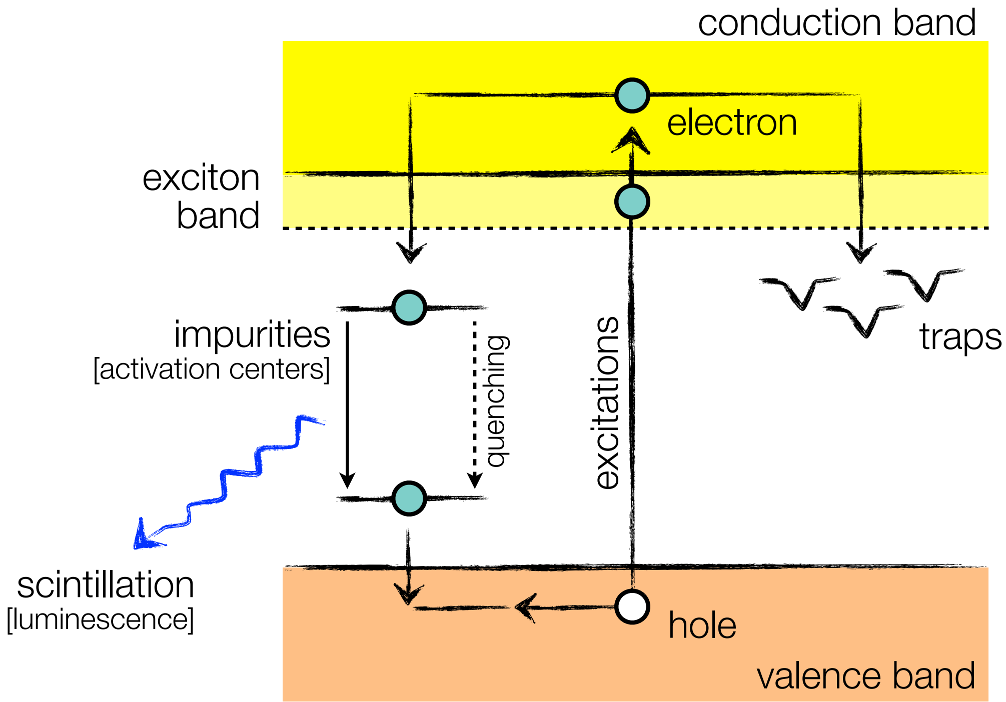

Energy bands in
impurity activated crystal
showing excitation, luminescence,
quenching and trapping

Inorganic Crystals

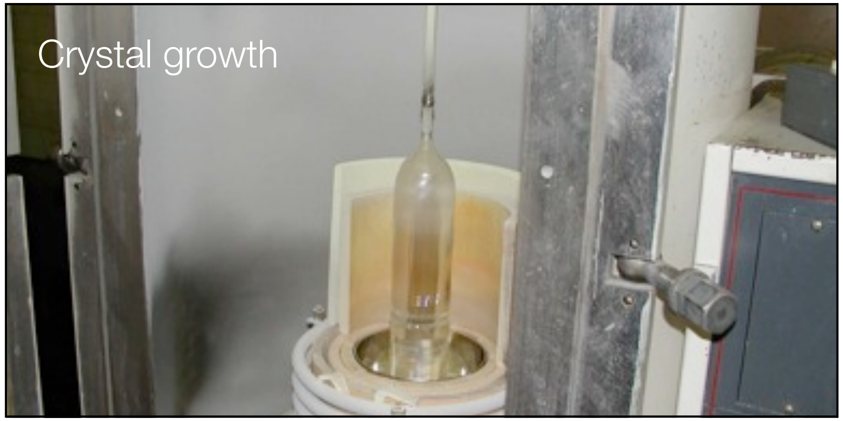

Example CMS
Electromagnetic Calorimeter

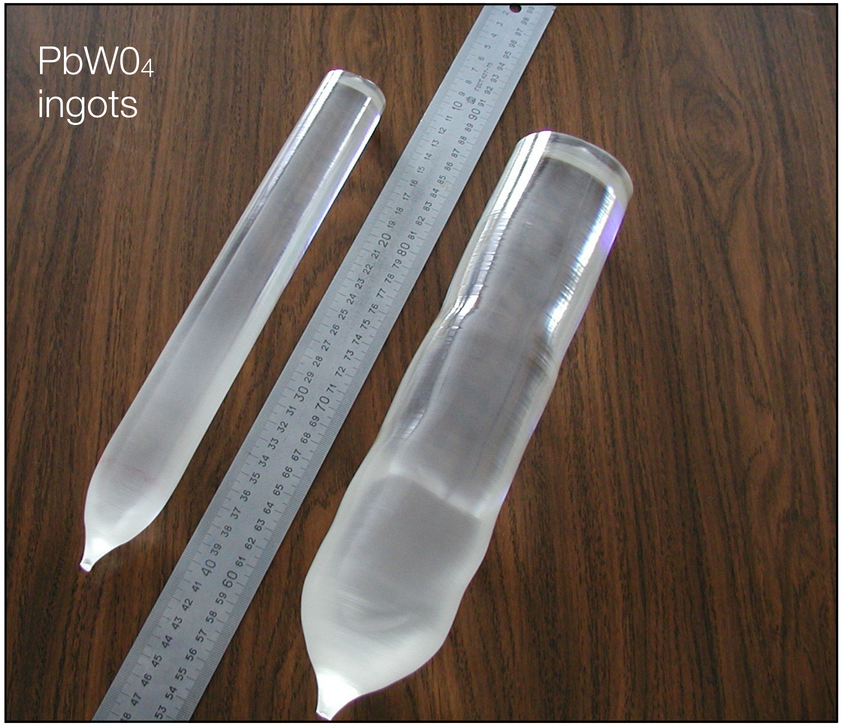

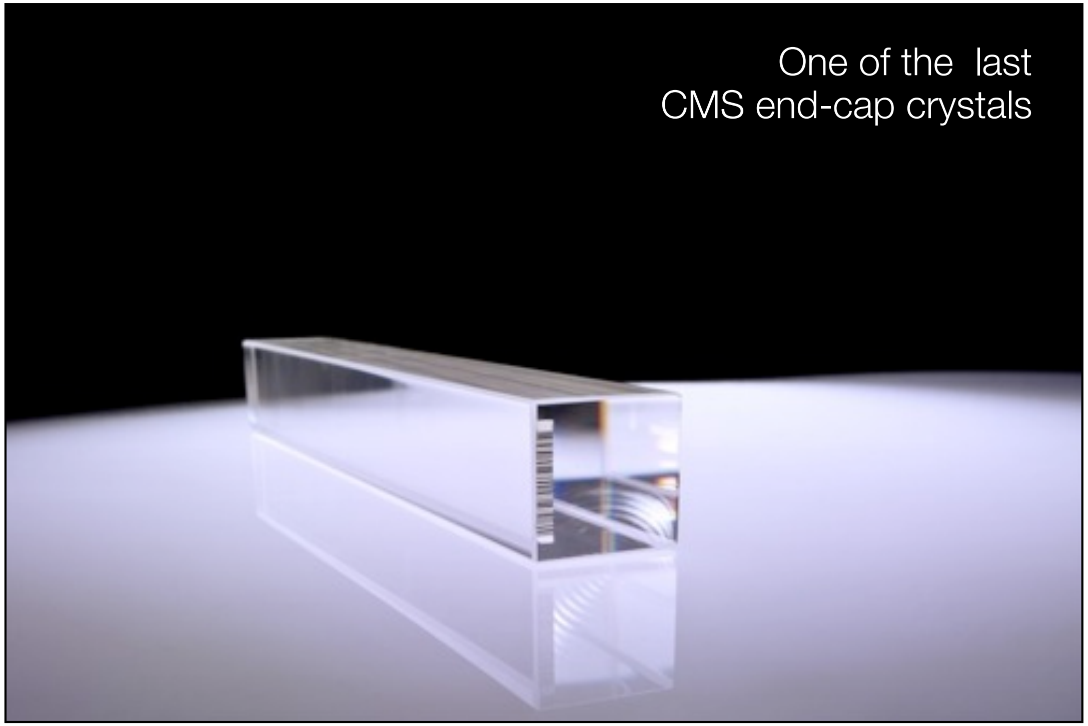

Inorganic Crystals – Time Constants

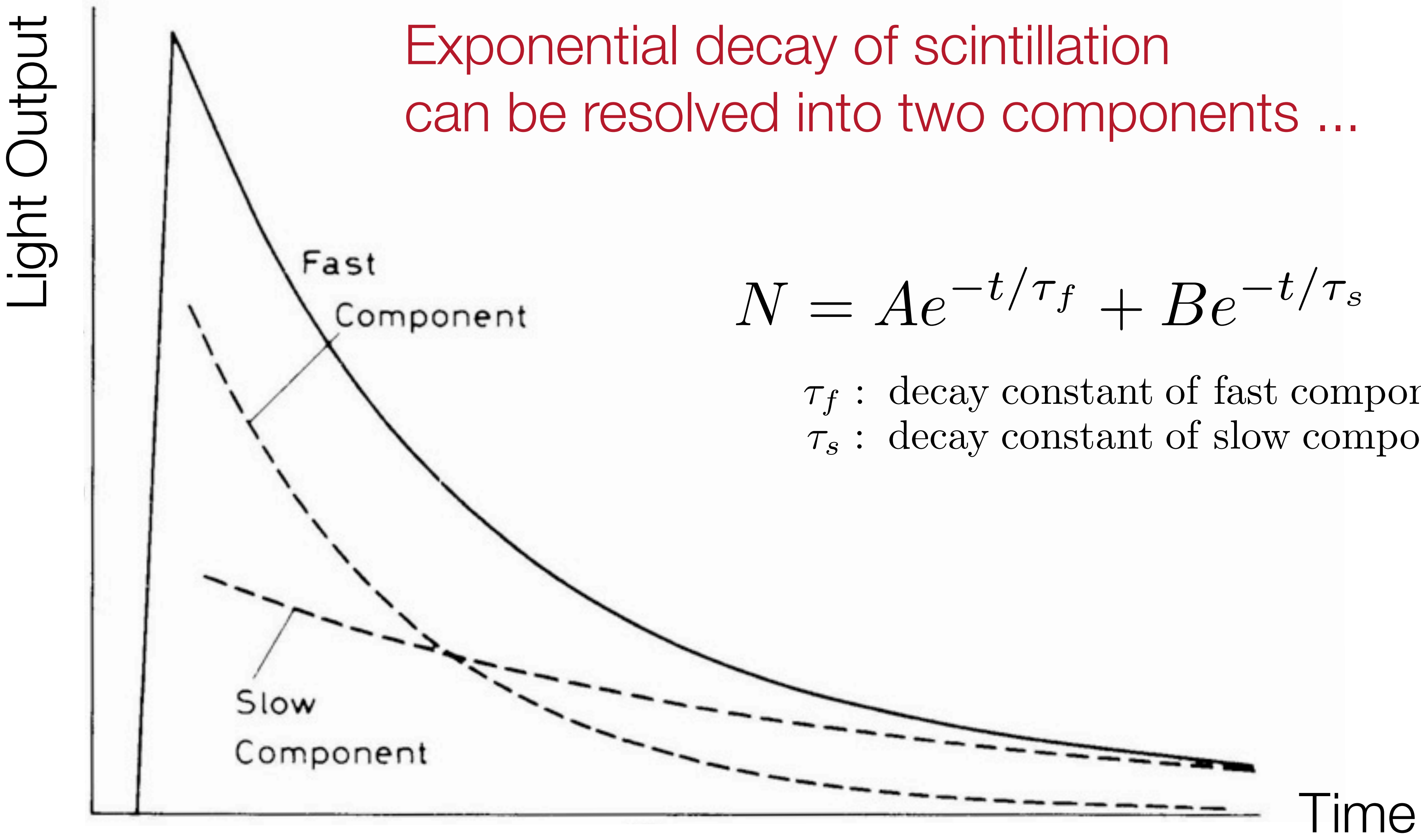

Exponential decay of scintillation
can be resolved into two components ...

$$N = Ae^{-t/\tau_f} + Be^{-t/\tau_s}$$

τ_f : decay constant of fast component
τ_s : decay constant of slow component

Inorganic Crystals – Light Output

Scintillation Spectrum
for NaI and CsI

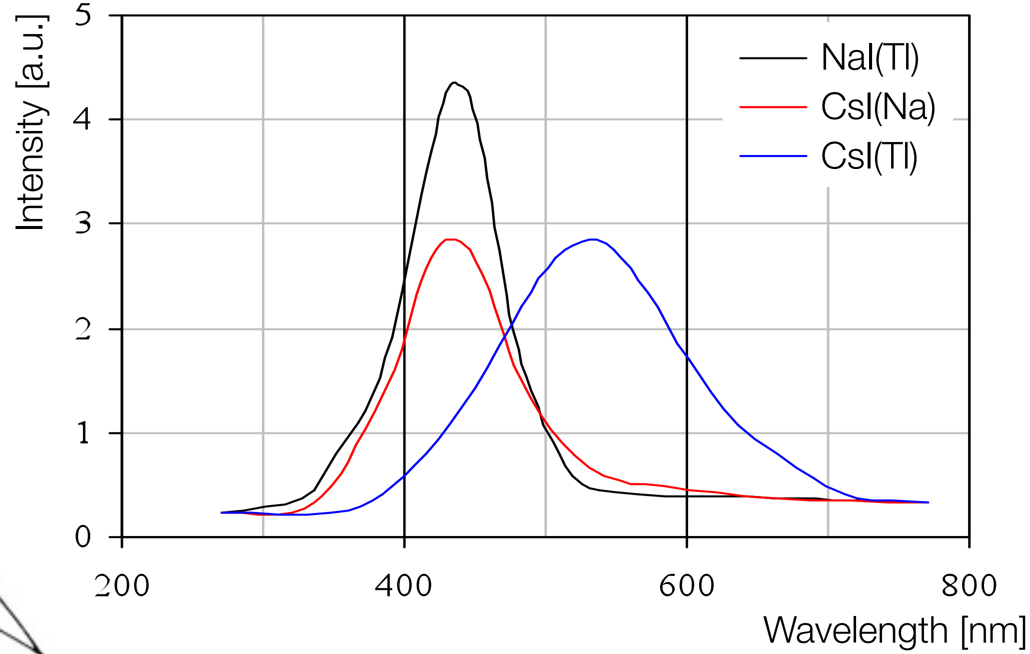

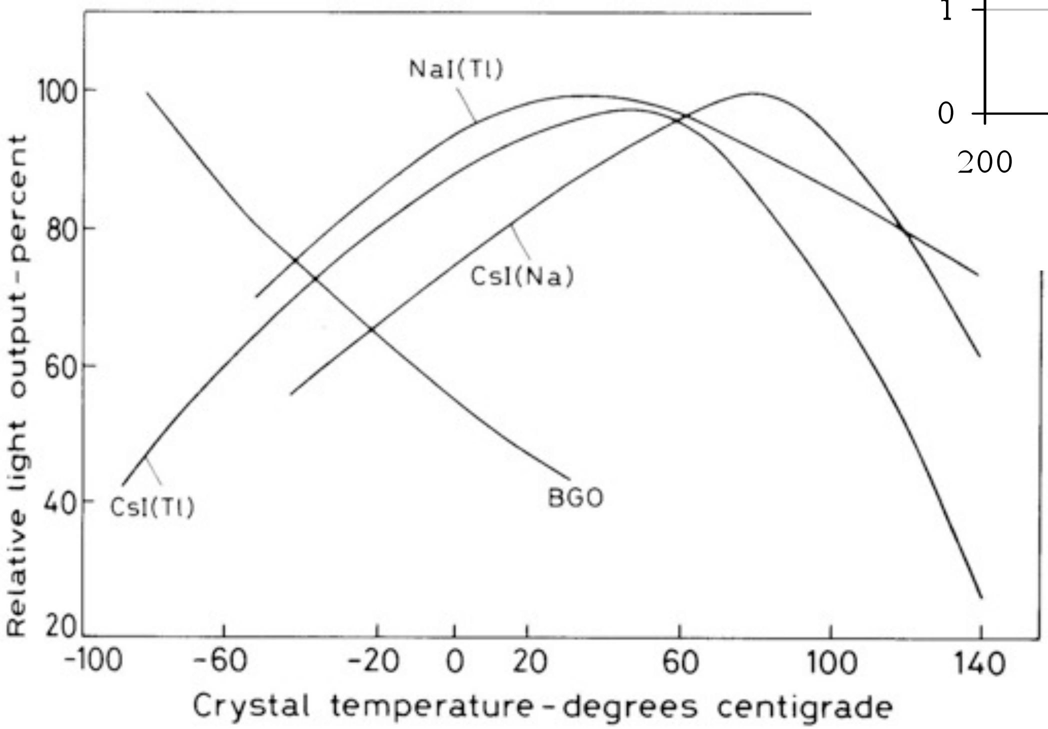

Strong
Temperature Dependence
[in contrast to organic scintillators]

Scintillation in Liquid Nobel Gases

Materials:

Helium (He)
Liquid Argon (LAr)
Liquid Xenon (LXe)
...

Decay time constants:

Helium : τ_1 = .02 μs, τ_2 = 3 μs
Argon : $\tau_1 \leq$ .02 μs

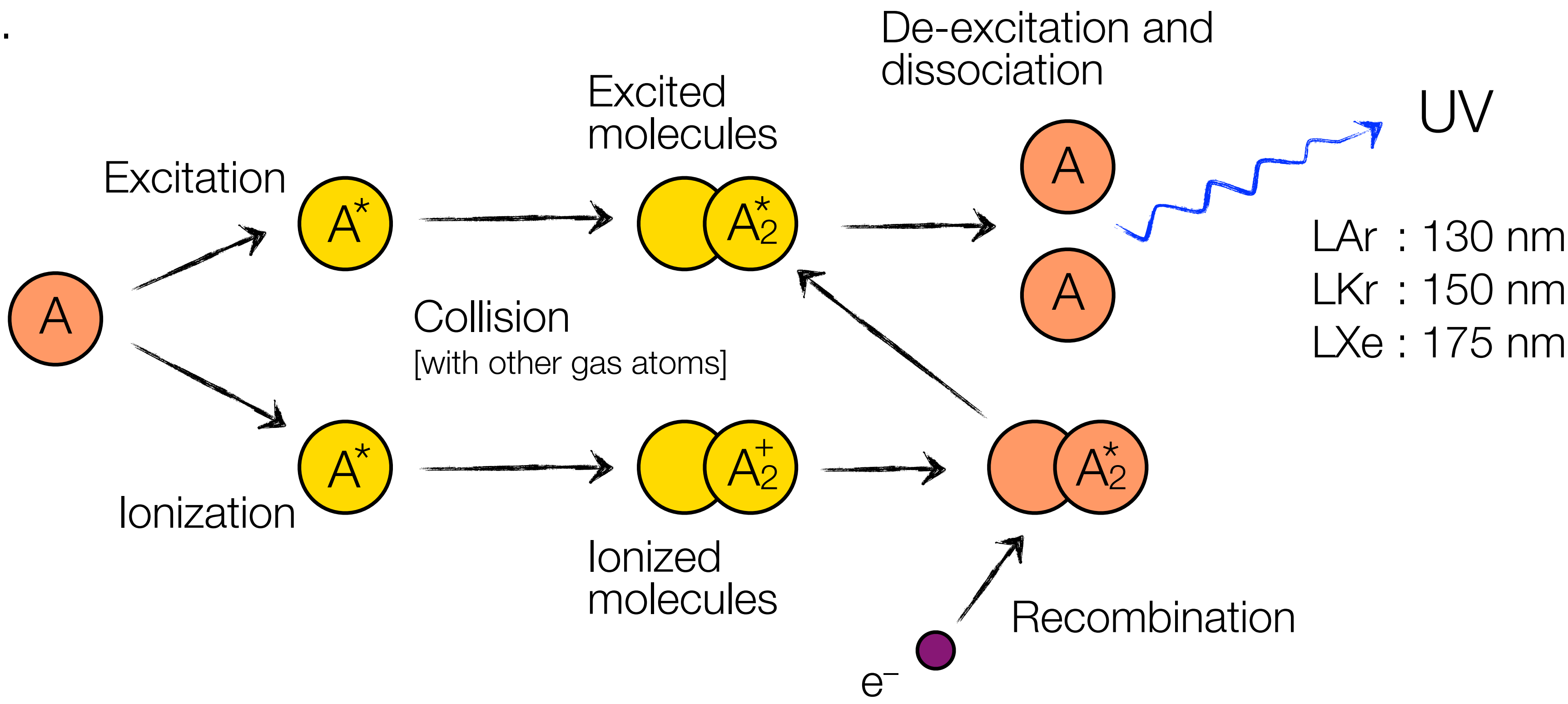

Inorganic Scintillators – Properties

Numerical examples:

NaI(Tl)

λ_{max} = 410 nm; hν = 3 eV
photons/MeV = 40000
τ = 250 ns

$PBWO_4$

λ_{max} = 420 nm; hν = 3 eV
photons/MeV = 200
τ = 6 ns

Scintillator quality:

Light yield – $\varepsilon_{sc} \equiv$ fraction of energy loss going into photons

e.g. NaI(Tl) : 40000 photons; 3 eV/photon ➛ $\varepsilon_{sc} = 4 \cdot 10^4 \cdot 3\ \text{eV}/10^6\ \text{eV} = 11.3\%$
$PBWO_4$: 200 photons; 3 eV/photon ➛ $\varepsilon_{sc} = 2 \cdot 10^2 \cdot 3\ \text{eV}/10^6\ \text{eV} = 0.06\%$

[for 1 MeV particle]

Organic Scintillators

Aromatic hydrocarbon compounds:

e.g. Naphtalene [$C_{10}H_8$]
Antracene [$C_{14}H_{10}$]
Stilbene [$C_{14}H_{12}$]
...

Very fast!
[Decay times of O(ns)]

Scintillation light arises from
delocalized electrons in π-orbitals ...

Transitions of 'free' electrons ...

Naphtalene

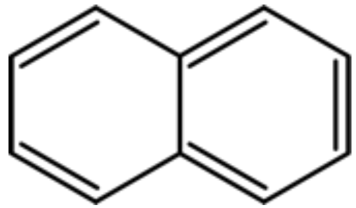

Antracene

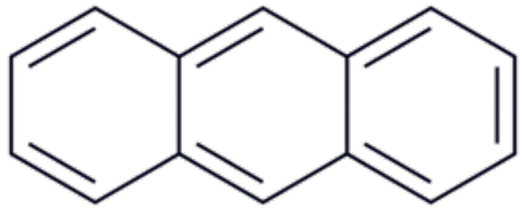

Scintillation is based on electrons of the C=C bond ...

π bond

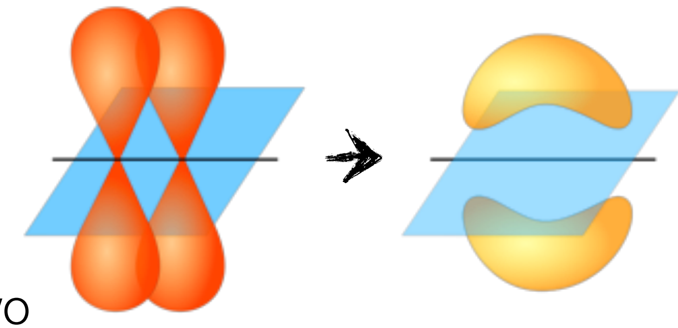

Two p_z orbitals

Organic Scintillators

Molecular states:

Singlet states
Triplet states

Fluorescence in
UV range
[~ 320 nm]

➥ usage of
wavelength shifters

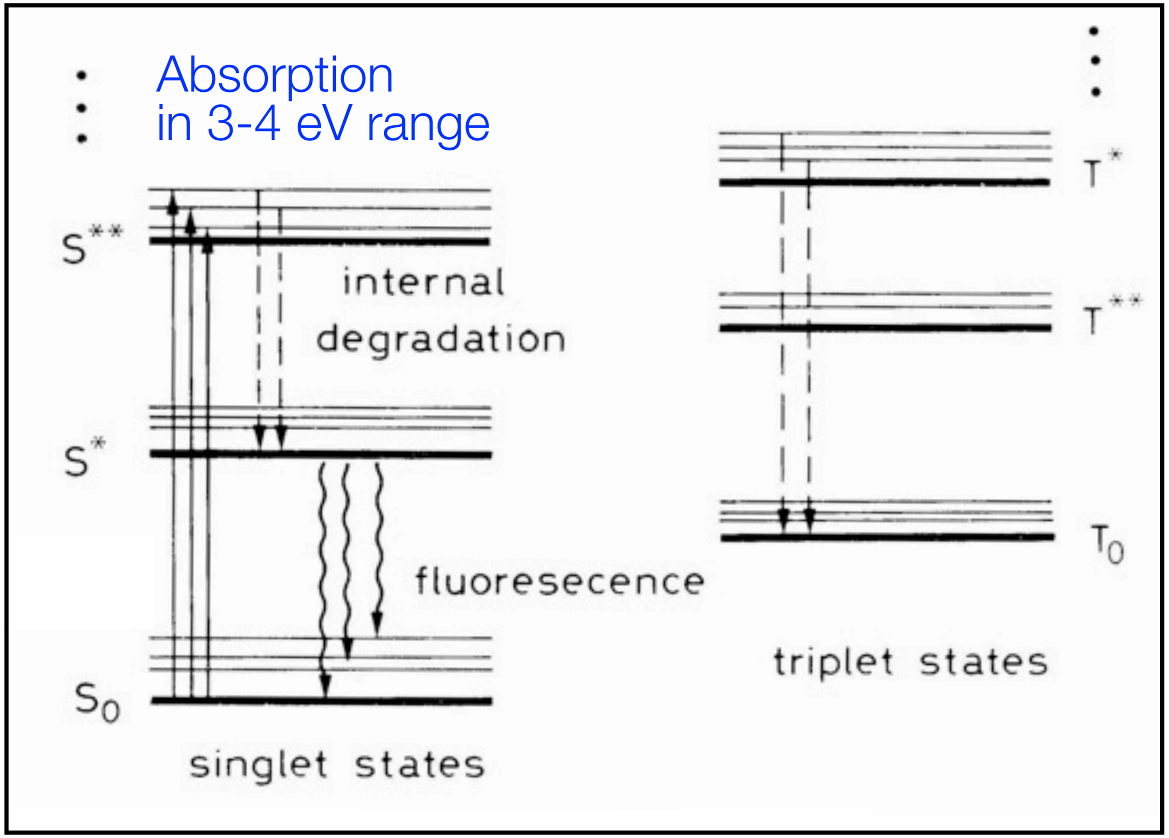

Fluorescence : $S_1 \rightarrow S_0$ [< 10^{-8} s]
Phosphorescence : $T_0 \rightarrow S_0$ [> 10^{-4} s]

Organic Scintillators

Transparency requires:

Shift of absorption
and emission spectra ...

Shift due to

Franck-Condon Principle

Excitation into higher vibrational states
De-excitation from lowest vibrational state

Excitation time scale : 10^{-14} s
Vibrational time scale : 10^{-12} s
S_1 lifetime : 10^{-8} s

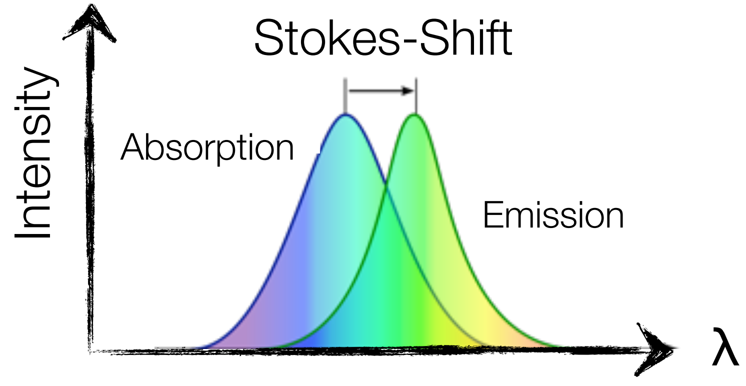

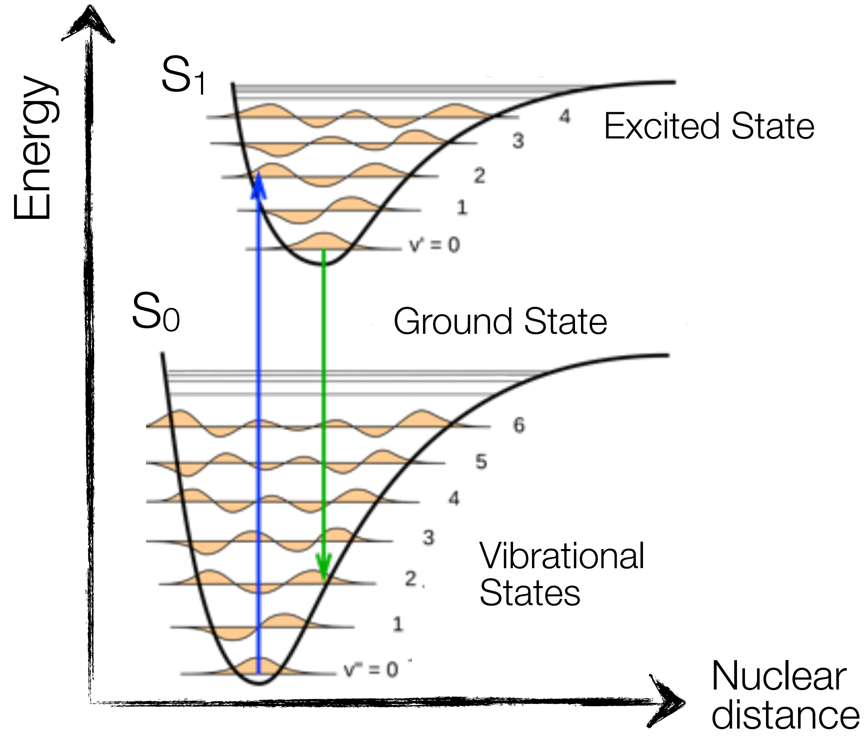

Plastic and Liquid Scintillators

In practice use ...

solution of organic scintillators
[solved in plastic or liquid]

+ large concentration of primary fluor
+ smaller concentration of secondary fluor
+ ...

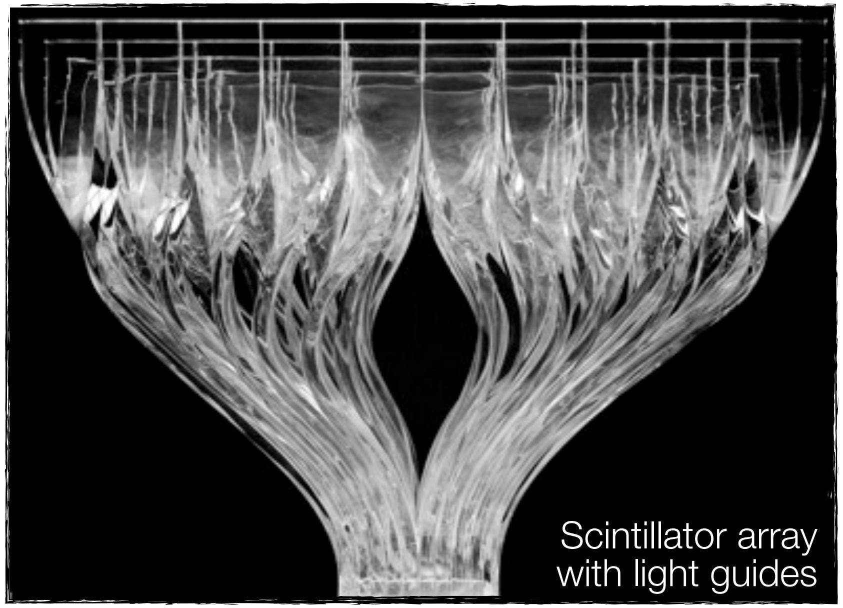

Scintillator array
with light guides

Scintillator requirements:

Solvable in base material

High fluorescence yield

Absorption spectrum must overlap
with emission spectrum of base material

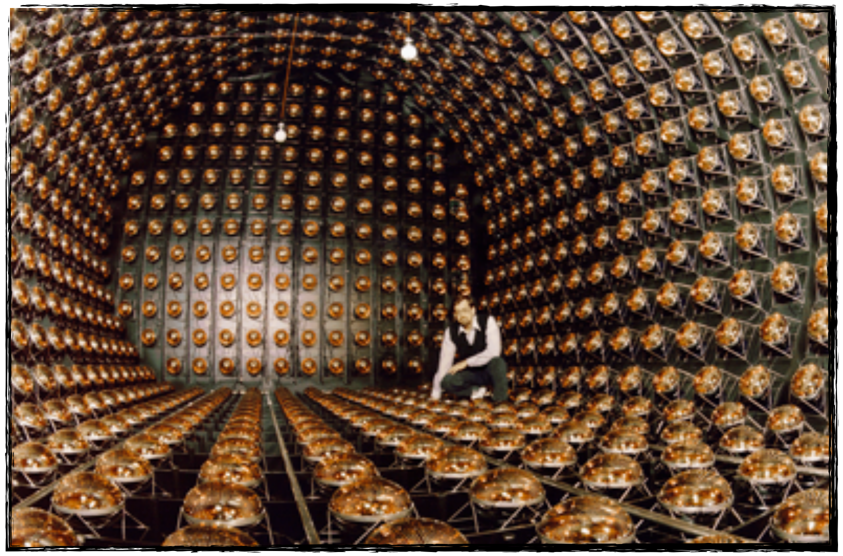

LSND experiment

Plastic and Liquid Scintillators

A

Energy deposit in base material ➛ excitation

Primary fluorescent

- Good light yield ...
- Absorption spectrum matched to excited states in base material ...

B

Secondary fluorescent

C

Wave length shifter

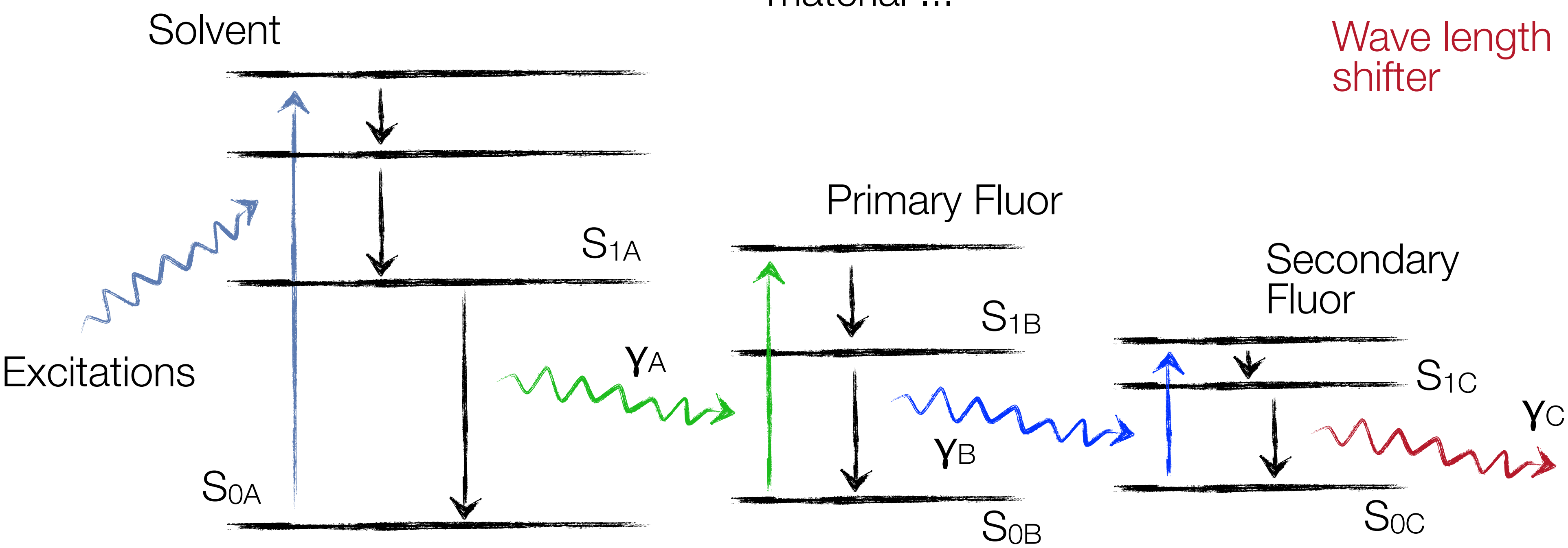

Wavelength Shifting

Principle:

Absorption of primary scintillation light

Re-emission at longer wavelength

Adapts light to spectral sensitivity of photosensor

Requirement:

Good transparency for emitted light

Schematics of wavelength shifting principle

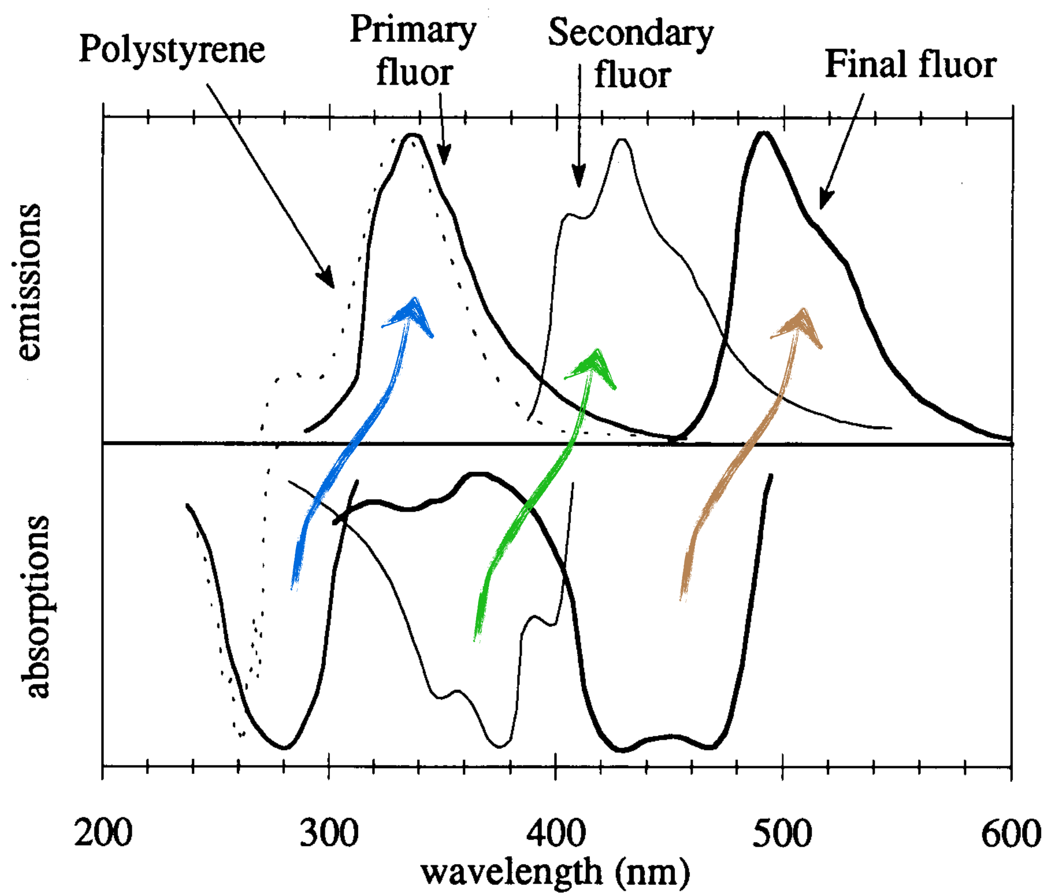

Organic Scintillators – Properties

Light yield:
[without quenching]

$$\frac{dL}{dx} = L_0 \frac{dE}{dx}$$

Quenching:
non-linear response due to saturation of available states

Birk's law:

$$\frac{dL}{dx} = L_0 \frac{\frac{dE}{dx}}{1 + kB\frac{dE}{dx}}$$

[kB needs to be determined experimentally]

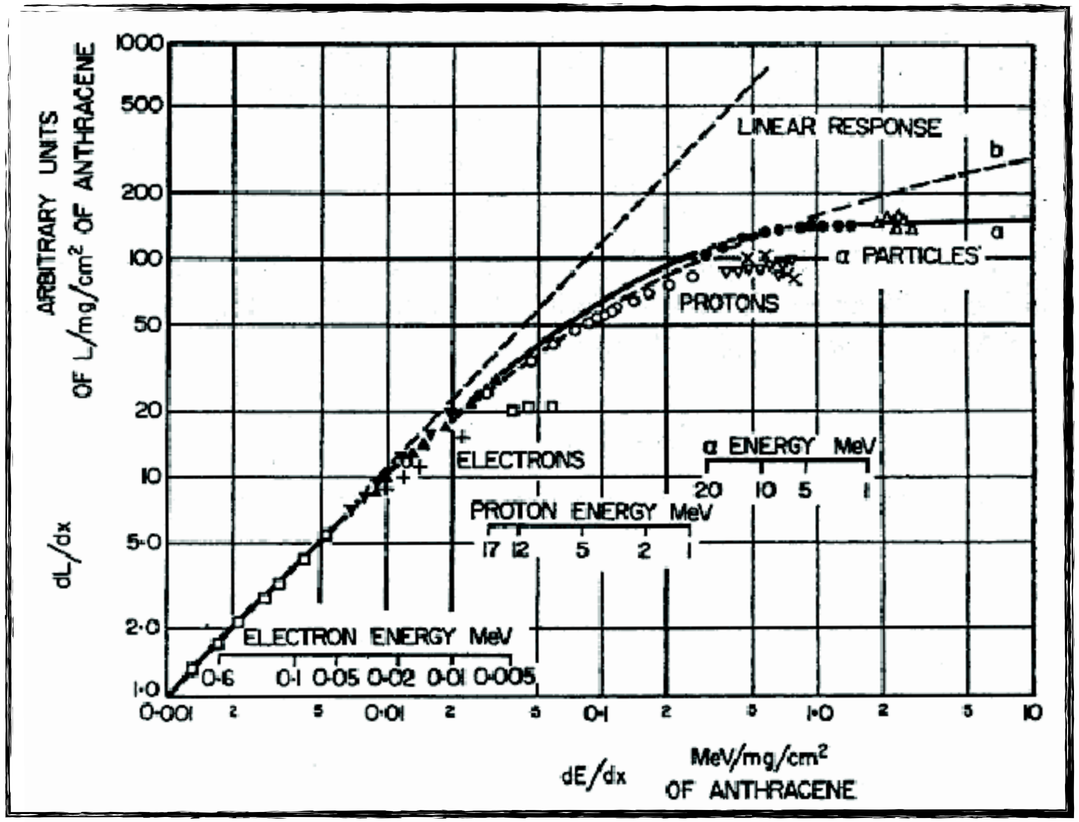

Also other parameterizations ...

Response different for different particle types ...

Scintillation Counters – Setup

Scintillator light to be guided to photosensor

➛ Light guide
[Plexiglas; optical fibers]

Light transfer by total internal reflection
[maybe combined with wavelength shifting]

Liouville's Theorem:

Complete light transfer impossible as $\Delta x\ \Delta\theta$ = const.
[limits acceptance angle]

Use adiabatic light guide like 'fish tail';

➛ appreciable energy loss

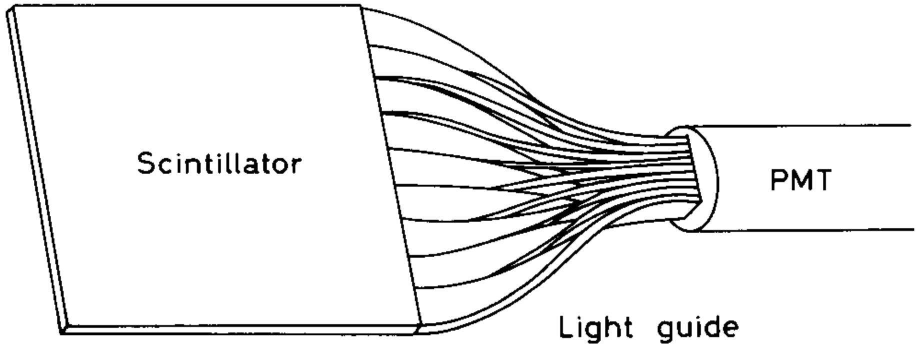

Light guide

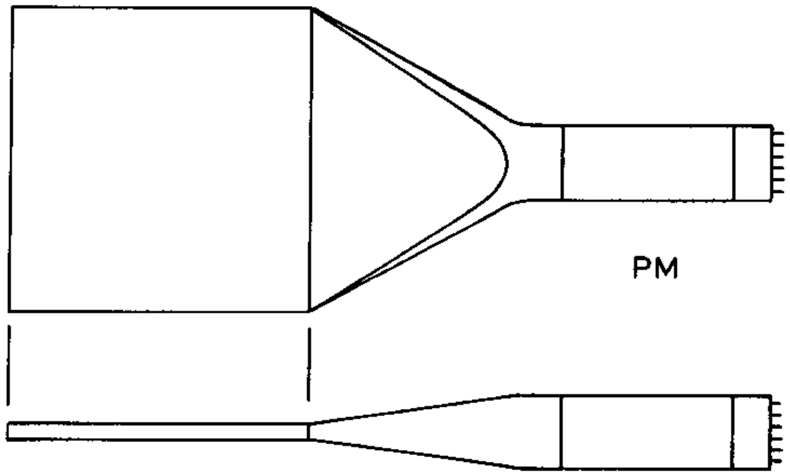

'fish tail'

Photon Detection

Purpose : Convert light into a detectable electronic signal
Principle : Use photo-electric effect to convert photons to photo-electrons (p.e.)

Requirement :

High Photon Detection Efficiency (PDE) or Quantum Efficiency; Q.E. = $N_{p.e.}/N_{photons}$

Available devices [Examples]:

Photomultipliers [PMT]
Micro Channel Plates [MCP]
Photo Diodes [PD]

HybridPhoto Diodes [HPD]
Visible Light Photon Counters [VLPC]
Silicon Photomultipliers [SiPM]

Photomultipliers – Dynode Chain

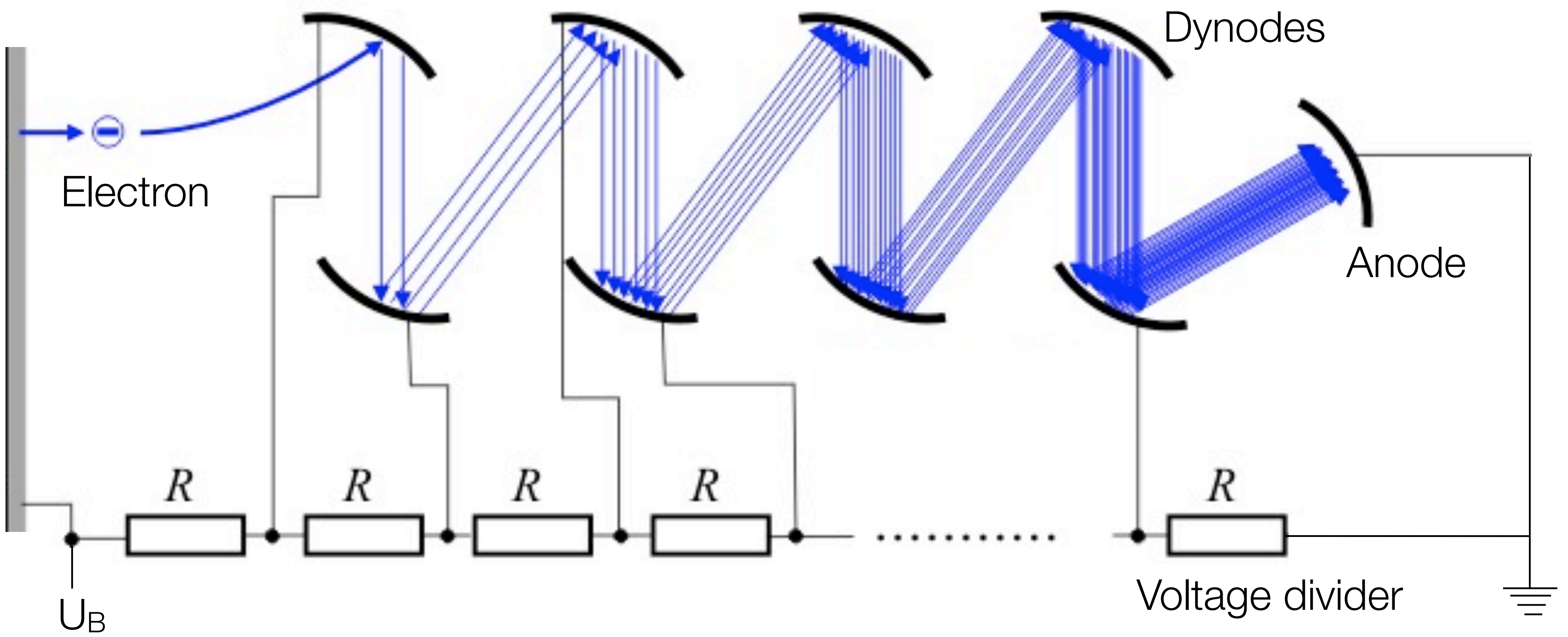

Multiplication process:

Electrons accelerated toward dynode
Further electrons produced ➛ avalanche

Secondary emission coefficient:
$\delta = \#(e^- \text{ produced})/\#(e^- \text{ incoming})$

Typical: $\left.\begin{array}{l}\delta = 2 - 10 \\ n = 8 - 15\end{array}\right]$ ➛ $G = \delta^n = 10^6 - 10^8$

Gain fluctuation: $\delta = kU_D$; $G = a_0 (kU_D)^n$

$dG/G = n\, dU_D/U_D = n\, dU_B/U_B$

Photomultipliers – Dynode Chain

Optimization of

PMT gain
Anode isolation
Linearity
Transit time

B-field dependence

PM's are in general
very sensitive to B-fields !

Even to earth field (30-60 μT).
μ-metal shielding required.

Venetian blind

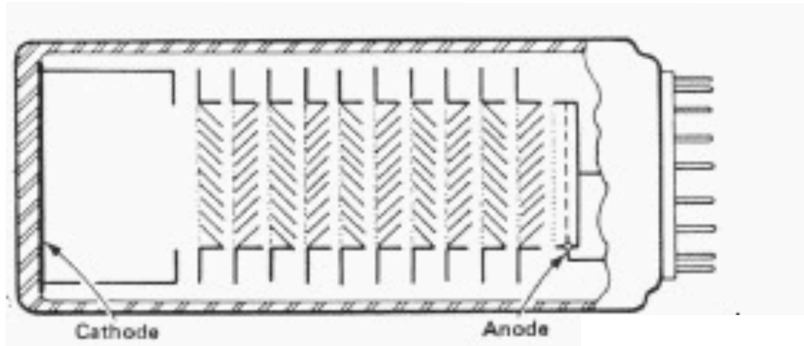

Box and grid

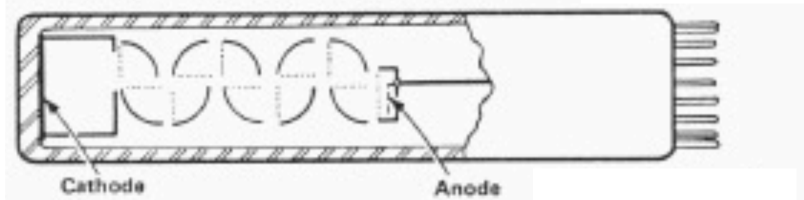

Linear focused

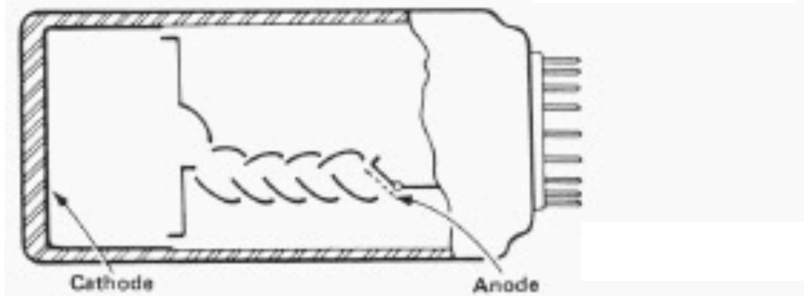

Circular focused

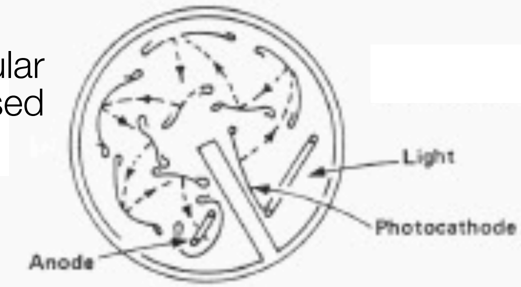

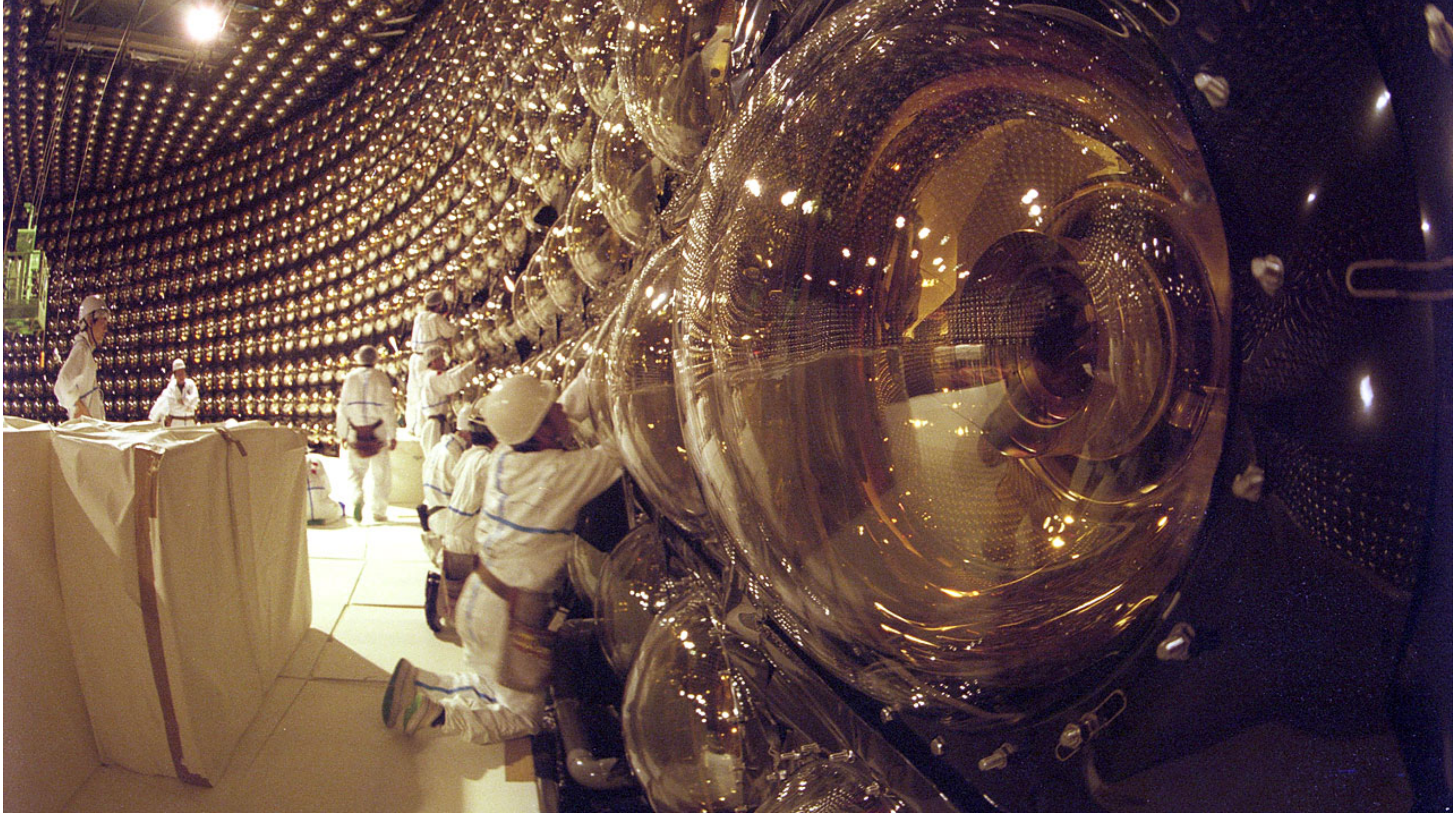

Super-Kamiokande neutrino observatory (Japan)
1 km underground
cylindrical stainless steel tank with 41.4 m height and 39.3 m diameter
11146 PMTs with 50 cm diameter

Photomultipliers – Photocathode

Bialkali: SbRbCs; SbK_2Cs

γ-conversion
via photo effect ...

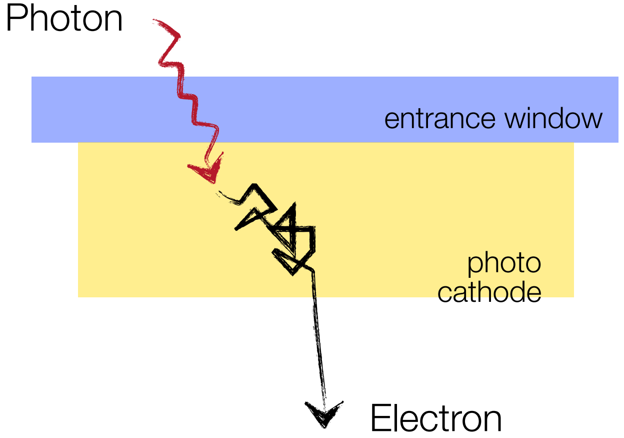

4-step process:

Electron generation via ionization
Propagation through cathode
Escape of electron into vacuum

Q.E. ≈ 10-30%
[need specifically developed alloys]

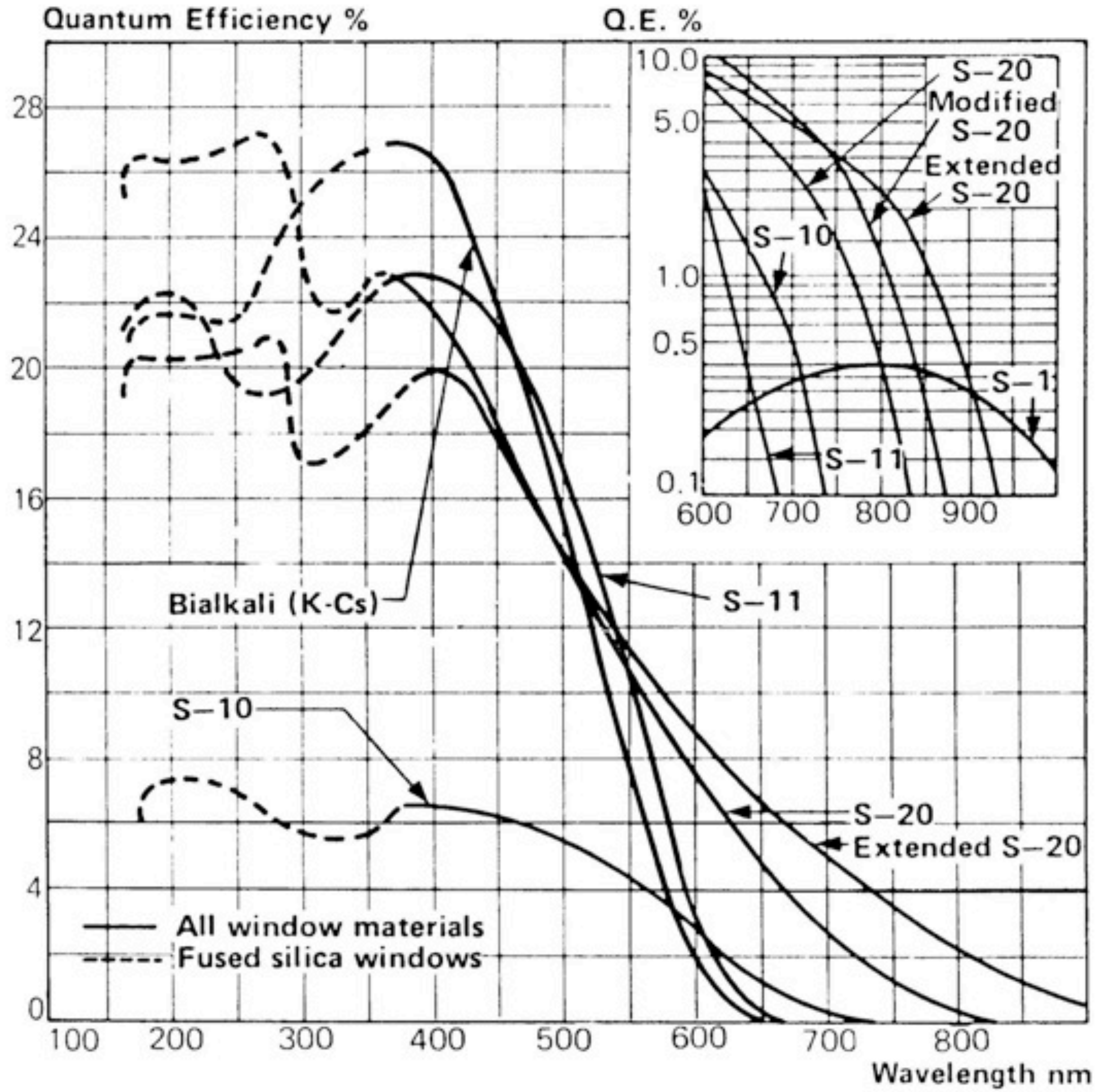

Photomultipliers – Energy Resolution

Energy resolution influenced by:

Linearity of PMT: at high dynode current possibly saturation by space charge effects; $I_A \propto n_\gamma$ for 3 orders of magnitude possible ...

Photoelectron statistics: given by poisson statistics.

$$P_n(n_e) = \frac{n_e^n \, e^{-n_e}}{n!}$$

with n_e given by dE/dx ...

$$\sigma_n / \langle n \rangle = 1/\sqrt{n_e}$$

light collection efficiency

$$n_e = \frac{dE}{dx} \times \frac{\text{Photons}}{\text{MeV}} \times \eta \times \text{Q.E.}$$

For NaI(Tl) and 10 MeV photon;
photons/MeV = 40000;
η = 0.2; Q.E. =0.25

$$n_e = 20000$$
$$\sigma_n / \langle n \rangle = 0.7\%$$

Secondary electron fluctuations:

$$P_n(\delta) = \frac{\delta^n \, e^{-\delta}}{n!}$$

$$\sigma_n / \langle n \rangle = 1/\sqrt{\delta}$$

with dynode gain δ;
and with N dynodes ...

$$\left(\frac{\sigma_n}{\langle n \rangle} \right)^2 = \frac{1}{\delta} + ... + \frac{1}{\delta^N} \approx \frac{1}{\delta - 1}$$

σ_n/<n> dominated by first dynode stage ...

... important for single photon detection